Multiscale characterisation of chimneys/pipes: Fluid escape structures within sedimentary basins

Adam H. Robinson [a],[*],[1], Ben Callow [a],[*],[1], Christoph Böttner [b], Naima Yilo [a],
Giuseppe Provenzano [a],[c], Ismael H. Falcon-Suarez [d], Héctor Marín-Moreno [d],[e],
Anna Lichtschlag [d], Gaye Bayrakci [d], Romina Gehrmann [a], Lou Parkes [f], Ben Roche [a],
Umer Saleem [g], Bettina Schramm [b], Malin Waage [h], Aude Lavayssière [a], Jianghui Li [a],
Farid Jedari-Eyvazi [a], Sourav Sahoo [d], Christian Deusner [b], Elke Kossel [b], Timothy A. Minshull [a],
Christian Berndt [b], Jonathan M. Bull [a], Marcella Dean [i], Rachael H. James [a], Mark Chapman [f],
Angus I. Best [d], Stefan Bünz [h], Baixin Chen [g], Douglas P. Connelly [d], Judith Elger [b],
Matthias Haeckel [b], Timothy J. Henstock [a], Jens Karstens [b], Calum Macdonald [f],
Juerg M. Matter [a], Laurence North [d], Benedict Reinardy [j]

[a] University of Southampton, School of Ocean and Earth Science, Southampton, SO14 3ZH, UK
[b] GEOMAR Helmholtz-Centre for Ocean Research Kiel, Kiel, Germany
[c] University of Grenoble Alpes, ISTerre, Grenoble, France
[d] National Oceanography Centre, Waterfront Campus, Southampton, SO14 3ZH, UK
[e] Norwegian Geotechnical Institute, PB 3930 Ullevål Stadion, NO-08906, Oslo, Norway
[f] University of Edinburgh School of Geosciences, Grant Institute, Edinburgh, EH9 3JW, UK
[g] Institute of Mechanical, Process and Energy Engineering, Heriot-Watt University, Edinburgh, EH14 4AS, UK
[h] UiT The Arctic University of Norway, Department of Geosciences, Tromsø, Norway
[i] Shell Global Solutions International BV, Grasweg 31, 1031 HW, Amsterdam, the Netherlands
[j] Stockholm University and Bolin Centre for Climate Research, Stockholm, Sweden

ARTICLE INFO

ABSTRACT

Evaluation of seismic reflection data has identified the presence of fluid escape structures cross-cutting overburden stratigraphy within sedimentary basins globally. Seismically-imaged chimneys/pipes are considered to be possible pathways for fluid flow, which may hydraulically connect deeper strata to the seabed. The properties of fluid migration pathways through the overburden must be constrained to enable secure, long-term subsurface carbon dioxide (CO_2) storage. We have investigated a site of natural active fluid escape in the North Sea, the Scanner pockmark complex, to determine the physical characteristics of focused fluid conduits, and how they control fluid flow. Here we show that a multi-scale, multi-disciplinary experimental approach is required for complete characterisation of fluid escape structures. Geophysical techniques are necessary to resolve fracture geometry and subsurface structure (e.g., multi-frequency seismics) and physical parameters of sediments (e.g., controlled source electromagnetics) across a wide range of length scales (m to km). At smaller (mm to cm) scales, sediment cores were sampled directly and their physical and chemical properties assessed using laboratory-based methods. Numerical modelling approaches bridge the resolution gap, though their validity is dependent on calibration and constraint from field and laboratory experimental data. Further, time-lapse seismic and acoustic methods capable of resolving temporal changes are key for determining fluid flux. Future optimisation of experiment resource use may be facilitated by the installation of permanent seabed infrastructure, and replacement of manual data processing with automated workflows. This study can be used to inform measurement, monitoring and verification workflows that will assist policymaking, regulation, and best practice for CO_2 subsurface storage operations.

* Corresponding authors.
  E-mail addresses: A.H.Robinson@soton.ac.uk (A.H. Robinson), Ben.Callow@noc.soton.ac.uk (B. Callow).
[1] These authors contributed equally

1. Introduction

1.1. Overview

Carbon dioxide (CO_2) capture and subsurface storage (CCS) within sedimentary basins has been identified as an effective solution for reducing anthropogenic CO_2 emissions in the atmosphere (IPCC, 2005; The Global CCS Institute, 2019). CCS must form a key component of present and future global climate policy, in order to meet anthropogenic greenhouse gas emission reductions of 80–95 % by 2050, and limit model predictions of likely warming of $<2\ ^{\circ}C$ relative to pre-industrial levels (IPCC, 2014). Requirements for wide-scale implementation of CCS include: 1) cost-effective CCS technologies; 2) government policy/incentives for negative emissions technologies; and 3) the need for public acceptance/confidence, all of which are intrinsically linked. The primary technological requirement to widespread implementation of CO_2 storage is subsurface site characterisation and containment assurance. Legal regulations governing CCS in Europe exist in the form of the EU CCS Directive on Geological Storage of Carbon Dioxide, 2009/31/EC (2009), which defines requirements for CO_2 storage across the lifetime of a storage site, including closure and post-closure obligations. Factors that must be considered for the characterisation and assessment of potential CO_2 storage complexes and their surroundings include the role and impacts of potential fluid migration pathways causing loss of containment, and the potential flux rates through these pathways.

CO_2 can be sequestered into porous and permeable subsurface sandstone reservoirs (Bachu, 2000; Benson and Cole, 2008), such as depleted oil and gas reservoirs and saline aquifers. Sandstone reservoirs of this type are commonly overlain by impermeable cap rocks and overburden stratigraphy, which together provide an effective seal that prevents the upward migration of CO_2, ensuring safe and permanent storage. Offshore CO_2 storage in sandstone reservoirs has been successfully demonstrated in Europe and globally (e.g., Sleipner, North Sea; Tomakomi, Japan). Several other commercial-scale offshore CO_2 storage projects are also in planning or development stages, such as the Northern Lights project (e.g., Furre et al., 2019a; Global CCS Institute, 2019).

The location and potential intensity of any possible loss of CO_2 containment from a storage reservoir is dependent on the distribution of fluid pathways in the cap rock and overburden, and the ability of these pathways to transmit dissolved, liquid, and/or gaseous CO_2, depending on the pressure-temperature conditions and presence of other fluids. Potential pathways may include anthropogenic sources, such as abandoned wells (e.g., Watson and Bachu, 2009), formation level inherent structures, including natural migration up-dip along permeable stratigraphic horizons (e.g., Tóth, 1980; Hindle, 1997), and the formation or reactivation of fluid escape structures (e.g., Nichols et al., 1994; Frey et al., 2009). Such fluid escape, or seal bypass, structures permit pressure-driven, focused fluid flow, which hydraulically connects deeper strata with the seafloor through inter-connected faults, fractures, and porous-permeable sediment layers (Cartwright et al., 2007). Fluid escape can take place as single blow-out events, episodic/pulsed flow, or as continuous seepage flow. The type of flow can vary depending on the subsurface pressure, stress, and lithological conditions. Therefore, the activity of a fluid escape structure may exhibit temporal variability, which may be cyclical over both short timescales such as tidal cycles (e.g., Boles et al., 2001) or longer-term sea level changes (e.g., Plaza-Faverola et al., 2011; Riboulot et al., 2014). Therefore, the combined understanding of the presence of fluid pathways and their fluid flow regime is critical for the risk assessment of potential subsurface CO_2 escape.

1.2. Aims & objectives

In this contribution we provide a broad overview of the integrated geophysical, geological, and geochemical methods which can be applied to the characterisation of focused fluid conduits. In order to achieve this, we use as our context an exemplar study of the fluid conduit beneath the Scanner pockmark, which we undertook as part of the European Union Horizon 2020 project Strategies for the Environmental Monitoring of Marine Carbon Capture and Storage (STEMM-CCS; http://www.stemm-ccs.eu), together with a partner project CHIMNEY (Characterisation of major overburden leakage pathways above sub-seafloor CO_2 storage reservoirs in the North Sea; Bull et al., 2018). STEMM-CCS and CHIMNEY focussed on determining the permeability of subsurface fluid pathways, and developing better techniques to locate fluid escape structures, so that they can be better quantified and constrained, with relevance to potential fluid flow at CO_2 storage complexes.

The paper has three main aims: (1) Firstly, we describe the various methods which may be applied to the characterisation of focused fluid conduits, and which allow us to resolve the physical parameters of interest (Section 3). For each individual method, we describe their capabilities, consider their benefits, address uncertainties, and deduce any further developments that may be required. In order to contextualise the various techniques which may be used, we describe their application during our investigation of the Scanner pockmark. (2) Secondly, we discuss the scales of imaging and resolution of the various methods described here, and the co-dependencies which exist between them. This permits integration into a multi-scale approach, and demonstrates how the different techniques may be employed in combination, to ensure appropriate constraint and calibration of the different methods, for complete characterisation of the fluid escape structures (Section 4). (3) Thirdly, based on our findings from this study, we describe a framework which can be used to determine the approaches that are needed to understand potential fluid flow structures in marine environments, in the context of the risk assessment of potential future CO_2 geological storage sites (Section 5).

2. Geological background

2.1. Focused fluid conduits in seismic data

Seismic chimneys (e.g., Hustoft et al., 2010) or pipes (e.g., Moss and Cartwright, 2010a), referred to hereafter only as chimneys, are observed in seismic reflection data as vertical to sub-vertical anomalies with circular or elliptical planforms, displaying seismic blanking and discontinuous or chaotic reflections (e.g., Løseth et al., 2011). Where free gas is present in the chimney, high amplitude seismic reflections, known as bright spots, with polarity reversals may be observed at discrete intervals, indicating gas accumulation during migration in layers of porous sediments (e.g., Ostrander, 1984). Pull-up of reflectors may also be observed, caused by high seismic velocities, which are commonly attributed to authigenic carbonate accumulations, or where located in the gas hydrate stability zone, to the presence of gas hydrate (e.g., Plaza-Faverola et al., 2010). If CO_2 migrates from a sub-seafloor storage reservoir and reaches the base of these chimneys, and if their permeability is sufficiently high, they could act as CO_2 pathways towards the seafloor and overlying water column. To provide a reliable prediction of potential seafloor seep sites, the degree to which these pathways are able to transmit fluids (i.e. permeability) needs to be better understood.

Chimneys have been globally observed by seismic imaging (e.g., Cartwright et al., 2007; Gay et al., 2007; Moss and Cartwright, 2010a, b; Løseth et al., 2011; Plaza-Faverola et al., 2017), including extensively in the North Sea (Hovland and Sommerville, 1985; Cole et al., 2000; Bünz et al., 2003; Karstens and Berndt, 2015; Böttner et al., 2019). A comprehensive analysis of 3D seismic reflection volumes in the South Viking Graben, North Sea (an area of 2850 km^2; Karstens and Berndt, 2015) identified 46 large-scale ($\sim100-1000$ m-wide) chimneys within the shallowest 1000 m of the overburden.

Chimney-like features can also be the result of seismic imaging artefacts. Seismic imaging artefacts may arise both as a result of data acquisition and/or processing (e.g., Tucker and Yorston, 1973). In particular, for locations where gas is present in the subsurface, the effect this has on seismic velocity determination can have a significant impact

on both time and depth migration. An example locality where a seismic artefact was interpreted as a chimney is the Goldeneye field, a prospective CO_2 storage site in the Central North Sea. Following high resolution 3D seismic processing a feature previously interpreted as a fluid escape conduit was later reinterpreted as a seismic imaging artefact caused by a glacial tunnel valley (Dean et al., 2015; Karstens and Berndt, 2015).

2.2. Formation of chimneys

Chimney formation was observed on a small scale during a controlled subsurface CO_2 release experiment known as QICS (Taylor et al., 2015; Cevatoglu et al., 2015). In this experiment, CO_2 was released into sediments at an increasing rate of 20–210 kg/day, at 12 m depth below the seabed in shallow water (5−30 m) in Ardmucknish Bay, Scotland. Repeated seismic reflection data acquisition prior to, during, and after the gas release showed the temporal development of a chimney, formed by gas propagating upwards by fracture generation and reactivation in fine grained sediment (Cevatoglu et al., 2015). Conditions for hydraulic fracture generation are favourable in shallow (low effective stress) unconsolidated, fine grained sediments, and may be considered a primary mechanism for chimney initiation (Fauria and Rempel, 2011). The upward propagation of fluids may also be facilitated by capillary driven invasion, most prevalent in conditions of high effective stress (Cathles et al., 2010). Further mechanisms for chimney genesis include: erosive fluidisation, localised subsurface volume loss, and syn-sedimentary formation (Lowe, 1975; Sun et al., 2013; Cartwright and Santamarina, 2015).

Based on the observations from QICS, and other experiments (e.g., Fauria and Rempel, 2011; Räss et al., 2018), a conceptual model for the formation mechanism and structure of chimneys in the shallow overburden has been developed (Bull et al., 2018). In this model, the first phase of formation is the hydraulic fracturing of low permeability sediments due to high fluid overpressure (Arntsen et al., 2007; Cartwright et al., 2007; Løseth et al., 2009). Seal breaching occurs due to reduced effective stress and leads to either opening of new fractures and/or reactivation of pre-existing fractures, generating a localised connected fracture system. These pathways may permit vertical buoyancy-driven migration of gas-rich pore fluids through the fracture network. Large-scale chimneys (~100−1000 m wide) are therefore hypothesised to represent a series of interconnected sub-vertical or radial fractures, which allow the vertical flow of gas in the shallow subsurface (Bull et al., 2018) due to the elevated permeability relative to the normal 'background' permeability of the host sediment (Cartwright et al., 2007). A transition from fracture to capillary dominant flow behaviour may be observed with increasing depth, due to increased overburden thickness (higher effective stress).

In addition to the role of the geometric structures of chimneys in governing fluid flow, coupled physical and chemical processes act within fractures and pores, resulting in complex feedback mechanisms between porosity-permeability and CO_2/CH_4 reactivity, which may affect the hydro-mechanical response of the system. From a quantitative perspective, little is known regarding the impact that chimneys have on the upwards migration of CO_2 and CH_4 to the seabed (Liu et al., 2019; Marín-Moreno et al., 2019).

2.3. Study area – Scanner pockmark

We have investigated an exemplar natural fluid escape system located near the centre of the Witch Ground Basin, located 190 km off the north-east coast of Scotland (Fig. 1a), within licence block 15/25 of the North Sea. Here, chimneys are observed, which underlie active natural methane venting sites at the seabed, within ~150 m water depth (Fig. 1b) - the Scanner, Challenger and Scotia pockmark complexes (Gafeira and Long, 2015). Pockmarks are seabed depressions, created by release of over-pressured pore-water and gas from the subsurface

(Hovland et al., 2010). In this area of the North Sea, large pockmarks (>6 m deep, >250 m long, and >75 m wide; class 1, Böttner et al., 2019) are continuously active. Evidence for active methane venting at the Scanner pockmark complex is provided by water column imaging and the presence of methane derived authigenic carbonates (MDACs) at the seabed (Judd et al., 1994; Judd and Hovland, 2009). The West Scanner pockmark (Fig. 1c) releases methane at 1600−2600 kg/day (Li et al., 2020), derived from a combination of biogenic and thermogenic sources (Clayton and Dando, 1996). Smaller pockmarks (class 2) are also distributed across the area (Fig. 1b) with a dominant NNE/SSW orientation (>1500 across 225 km^2) and are interpreted as dewatering features attributed to localised pressure changes (Böttner et al., 2019). The Scanner pockmark complex overlies an area that has been appraised for CO_2 storage potential, the East Mey Storage Site (ACT Acorn Consortium, 2018).

2.3.1. Stratigraphy and seismostratigraphic framework

The lithostratigraphy and seismostratigraphic framework of the ~600 m-thick Quaternary sediment succession containing the Scanner pockmark complex was described by Böttner et al. (2019) and Stoker et al. (2011) (Fig. 2). Deposited within the Witch Ground Basin (Andrews et al., 1990), this complex is underlain by the Hordland and Nordland Groups, of Palaeogene and Neogene age respectively, and which are composed of claystone with limestone and sandstone interbeds (Judd et al., 1994).

The basal Quaternary unit, the Aberdeen Ground Formation (Fm.; unit S1 in Fig. 2), is composed of clay-rich sediments deposited in the Early Pleistocene (up to Marine Isotope Stage, MIS, 13), and displays a laterally continuous, layered seismic character (Stoker et al., 2011; Ottesen et al., 2014). The overlying Ling Bank Fm. (S2) erodes into the top of the Aberdeen Ground Fm., representing a regional glacial unconformity, with deposition of glacial tills in the Early to Middle Pleistocene (~1.2−0.5 Ma, MIS 12 to 10; Stewart and Lonergan, 2011; Reinardy et al., 2017; Böttner et al., 2019). The glacial tunnel valleys of the Ling Bank Fm. display both a layered and non-layered seismic character. The Coal Pit Fm. (S3) overlies the Ling Bank and Aberdeen Ground Fms., and comprises glacial tills (which include pebbly and muddy sands) deposited in the upper Mid to Late Pleistocene (MIS 6-3; Andrews et al., 1990; Stoker et al., 2011). The Coal Pit Fm. is conformably overlain by Last Glacial Maximum (LGM) deposits, which comprises silty-sandy clays with rare pebbles, deposited during MIS 3−2 (S4). Unit S4 extends upwards to the base of Scanner pockmark. The Coal Pit Fm. and LGM deposits have a dim and chaotic seismic character and are conformably overlain by the Witch Ground Fm. (S5), composed of silty clay deposited during MIS 2 to 1 (Stoker et al., 2011). The Witch Ground Fm. has two main units: the lower (S5.1) and upper (S5.2) Witch Ground Member respectively. The lower Witch Ground Member has an apparent interbedded seismic character. The upper Witch Ground Member conformably overlies the lower Witch Ground Member, thinning or pinching out towards the northeast. The upper Witch Ground Member is composed of sediments of Holocene age (MIS 1) and has a uniform seismic character (Stoker et al., 2011). The Scanner pockmark depression erodes down to the base of the lower Witch Ground Member.

3. Overview of chimney characterisation methods

3.1. Overview & data acquisition

The methods used to investigate chimneys and their associated fluid flow can be divided into several types (Table 1). These include: seismic reflection imaging, ocean-bottom seismic methods, including seismic tomography and anisotropy analysis, controlled source electromagnetic surveying (CSEM), active acoustics, passive seismic monitoring, sediment sampling of both the target site and onshore analogues, laboratory rock physics experiments, and process-based numerical modelling and fluid dynamic modelling approaches.
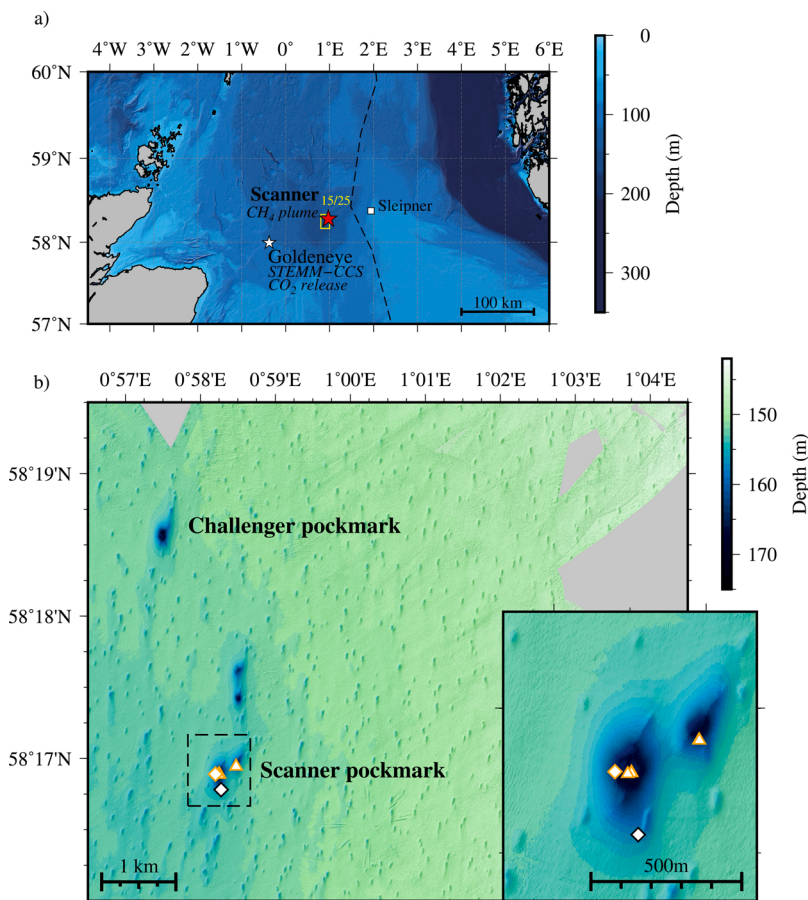
Fig. 1. STEMM-CCS and CHIMNEY study area. a) Regional map of northern North Sea plotted over GEBCO (2019) bathymetry. Location of the Scanner and Goldeneye experiment sites and active Sleipner CCS storage site are labelled. Yellow box indicates location of UK North Sea licence box 15/25. Dashed black line demarcates boundary between UK (to W) and Norway (to E) exclusive economic zones (200 nm). b) Ship-acquired swath bathymetry of the study area, around Scanner and Challenger pockmark complexes. Dashed black box indicates location of inset. Inset: Detailed bathymetry of Scanner pockmark complex. Diamonds and triangles indicate locations of RD2 drilling locations and gravity coring sites respectively. Orange outline indicates acquisition during cruise leg MSM78. Black outline indicates acquisition during cruise leg POS518.

In support of the STEMM-CCS and CHIMNEY projects, four research expeditions were undertaken for data collection at the Scanner pockmark complex. 2D seismic reflection and refraction data, for use in travel time tomography, were acquired using a GI gun source and 18 ocean bottom seismographs (OBS) by RV Maria S Merian cruise MSM63 (Fig. 3a,d; Berndt et al., 2017), in addition to multi-beam bathymetry data, controlled source electromagnetic (CSEM) data (Fig. 5), and Parasound sub-bottom profiling data (Fig. 2a). RRS James Cook cruise JC152 conducted a wide-ranging seismic experiment over the Scanner and Challenger pockmarks (Figs. 3 & 4). Five different seismic sources were used (Bolt and GI airguns, Squid and Duraspark surface sparkers, and a deep towed sparker; Fig. 3), which were recorded by arrays of 25 and 7 OBSs, at the Scanner and Challenger pockmarks respectively (Fig. 3a; Bull, 2017). The seismic sources were also used to generate multichannel (GI guns, surface sparkers; Fig. 2b) and single channel (deep tow sparker) seismic reflection profiles. During cruises MSM78 (Karstens et al., 2019) and RV Poseidon POS518-2 (Linke and Haeckel, 2018), sediment cores for geological and geochemical analysis were taken from within the Scanner pockmark and a reference site (Fig. 1b,c) using a gravity corer and rock drill (RD2), which acquired core to depths of ~6 and ~33 m below seafloor (mbsf) respectively. Additionally, data from a 3D seismic survey conducted by PGS (Fig. 2c; CNS Mega Survey Plus) were used to further support the study.

3.2. Seismic reflection methods

3.2.1. Introduction

Multichannel seismic reflection data record the wavefield reflected from physical discontinuities in the subsurface at a range of distances from an active source of acoustic energy. By doing so, they carry information about seismic wave propagation velocity and anomalies in

visco-elastic properties. So long as the geological boundaries correspond to changes in physical properties controlling seismic wave propagation, reflection data imaging provides us with a representation of subsurface sedimentary and tectonic structures with a resolution equal to a fraction of the propagated wavelength (Kallweit and Wood, 1982). Sub-vertical fluid escape structures and sediment deformation (e.g., sediment mobilisation and polygonal faulting) can therefore be imaged, potentially also allowing for a relative dating of geological events by interpreting cross-cutting structures and stratal stacking patterns.

Changes in pore fluid type, especially partial gas saturation, have a strong influence on seismic velocities and the absorption of seismic wave energy (White, 1975; Domenico, 1977). The bulk effect of gas accumulation within sediment pores is a reduction in the sediment compressibility and, therefore, acoustic impedance (Tóth et al., 2014). Typically this results in strong acoustic impedance contrasts, visible in the seismic data as negative polarity reflections known as bright spots (Cevatoglu et al., 2015). More generally, pore gas manifests itself as local increments in the subsurface reflectivity, as a function of the properties of the encasing medium and the local partial gas saturation (Berndt, 2005; Cartwright, 2007; Løseth et al., 2009; Andresen, 2012; Karstens and Berndt, 2015). Frequency-dependent attenuation and velocity dispersion can also be observed in ultra-high-frequency (in the order of kHz) data, as the seismic frequency approaches the gas bubble characteristic frequency, allowing the detection of gas migration irrespective of the presence of reflective anomalies (Tóth et al., 2015). Therefore, not only do reflection data allow us to image potential gas migration pathways in the subsurface, but also to detect gas accumulation pockets and potentially quantify their volume.

However, as a consequence of the strong energy partitioning at the interface with gas-charged sediments, acoustic blanking may be observed within chimneys (Fig. 2b,c; Fader, 1997), which hampers the
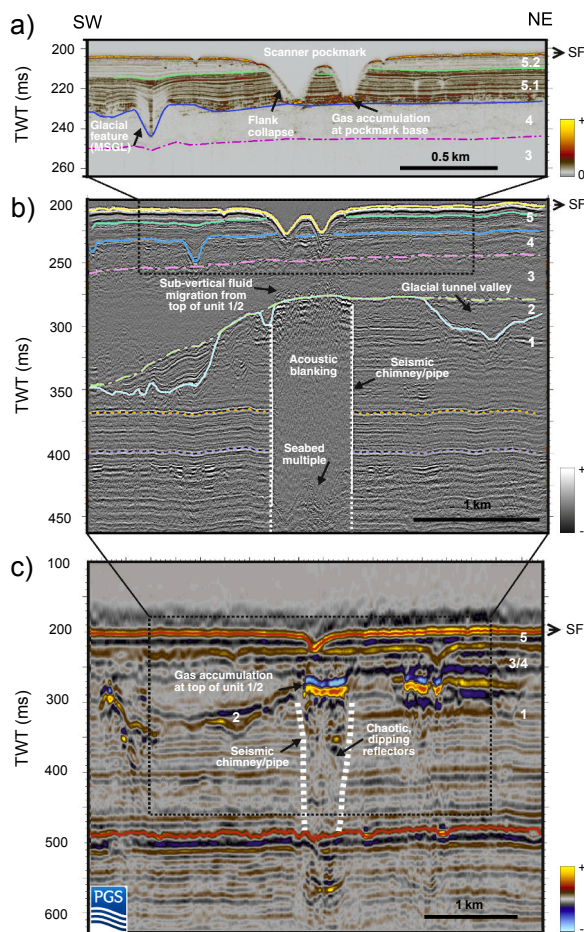
Fig. 2. Seismic stratigraphy of the Scanner pockmark region, after Böttner et al. (2019). Profiles shown extend from southwest to northeast across the Scanner pockmark complex. a) Sub-bottom profiler seismic reflection data. b) 2D seismic reflection data acquired using Sparker source. c) 3D seismic reflection data. Interpreted seismic units S1 to S5 are shown. S1 – Aberdeen Ground Fm., S2 – Ling Bank Fm., S3-4 – Coal Pit Fm. (S3 – Coal Pit & S4 – Last Glacial Maximum deposits (LGM)), S5 – Witch Ground Fm. (S5.1 – lower Witch Ground Member, S5.2 – upper Witch Ground Member). Light blue line = top S1; green dashed line = top S2; pink dashed line = top S3; blue line = top S4; green solid line = top S5.1 and yellow line = top S5.2 / SF = Seafloor. Outline of a chimney is displayed with white dashed line.

effectiveness of seismic reflection imaging and inversion in such contexts. As a result, wide-angle transmission data recorded at the seabed, for example on OBS, may also be required, in order to characterise seismic velocities below the gas layer. Wide-angle transmission also helps resolve the issue of ambiguity between the position of the reflector and the true interval velocity along the wave-path, since the short offset range and the limited bandwidth of seismic reflection data result in a limited sensitivity to interval velocities (Jannane et al., 1989). Therefore, integration with diving wave travel time tomography, in addition to reflection waveform inversion techniques (e.g., Brossier et al., 2015) and seismic-to-well calibration are necessary to compensate for the lack of sensitivity to the kinematic properties of the medium, and provide an accurate depth representation.

3.2.2. 2D vs 3D seismic reflection

Two-dimensional (2D) seismic imaging assumes that subsurface properties are invariant with respect to the direction normal to the survey line. In the case of inherently three-dimensional structures, such

as pockmarks and chimneys, this assumption represents a potentially significant source of error. Whilst a chimney can be assumed, in a simple case, to be radially symmetrical around the depth axis, there potentially may be out-of-plane reflections that affect imaging. Three-dimensional (3D) seismic data have substantially advanced the knowledge of sub-surface fluid migration features, which were previously often discarded as poorly imaged zones and seismic artefacts in 2D seismic data (Cartwright and Huuse, 2005). The analysis of 3D seismic data is an effective method to map fluid accumulations in the subsurface, identify permeability barriers, and constrain subsurface geometries of entire fluid flow systems (Cartwright et al., 2007; Løseth et al., 2009; Andresen, 2012; Karstens and Berndt, 2015). Where only 2D seismic data are available, application of 3D processing of 2D acquisition geometries (e.g., Lin et al., 2019) has proved extremely useful for improving the quality of the final results, provided that variations of the streamer position during acquisition are monitored within the desired accuracy (Whiteside et al., 2013) or estimated from the data (Clay and Vardy, 2018).

However, the resolution of conventional seismic data, laterally (often above 12.5 m) and vertically (~10 m for a dominant frequency of 40 Hz), is often not sufficient to image the seismic expression of fluid flow systems in detail. Recent developments in 3D high-resolution seismic techniques allow imaging of the shallow subsurface in much greater detail than previously (e.g., Planke et al., 2009; Petersen et al., 2010; Plaza-Faverola et al., 2015). An example technology is the P-Cable (e.g., Planke et al., 2009), which has been used to map shallow gas accumulations, gas hydrate systems, and fluid flow structures, such as chimneys (e.g., Plaza-Faverola et al., 2011; Bünz et al., 2012) down to a resolution of 3 m. In contrast to conventional seismic frequencies of ~5–120 Hz (suitable for monitoring deep reservoirs), high resolution P-Cable uses frequencies of up to 350 Hz, surpassing the resolution of conventional 3D seismic.

Collectively, the seismic experiments conducted at the Scanner pockmark complex utilise different imaging resolutions and depths, by applying a multiple-frequency 2D surveying approach using a number of seismic sources (Fig. 3b; Bull et al., 2018). Progressive extension of the seismic bandwidth to higher frequencies and shorter shot intervals results in higher vertical and lateral resolution. Surface sparker, deep towed sparker, and sub-bottom profiler data (the latter is single-channel, and may be considered a hydro-acoustic technique, but we include it here with the other seismic approaches as it is used for the same purpose) with frequencies up to several kHz reveal near surface structural features previously not discernable using lower frequency sources, such as sediment slumping/flank collapse within the pockmark, more detailed characterisation of gas accumulation at the top of the Aberdeen Ground Fm., and direct observation of fluid migration towards the base of the pockmark (Fig. 3a,b). Therefore, multi-frequency surveys with different sources (e.g., Bolt Gun, GI Gun, Chirp, Boomer, and Sparker) and high-resolution 2D or P-cable streamers can complement conventional 3D seismic data (e.g., Fig. 3c) and lead to a better understanding of the nature and internal architecture of chimneys, particularly in the shallow overburden stratigraphy.

3.2.3. Advanced seismic wavefield analysis

In addition to providing reflectivity images of the subsurface, multi-channel seismic data attributes, such as amplitude as a function of offset, can also be exploited to infer kinematic and dynamic properties of the subsurface (Ostrander, 1984). Pre-stack waveform inversion techniques (Virieux and Operto, 2009) can be applied to obtain quantitative characterisation of the effect of partial gas saturation on the elastic properties (P-wave velocities and Poisson's ratio). In particular, partial gas saturation has a strong effect on bulk modulus, associated with a relatively low influence on shear modulus, which corresponds to a lowering in P-wave impedance and a reduction of V_p/V_s ratio (Ostrander, 1984; Tóth et al., 2014; Provenzano et al., 2018). These contrasts can in turn be exploited to quantify gas accumulation using appropriately calibrated rock-physics models (Tóth et al., 2014; Provenzano et al., 2018).

Table 1

Summary of the methods used for the characterisation of a chimney, displaying the assessed parameters and the method specific traits. The parameters used for complete characterisation of a chimney include: 1) fracture geometry, orientation, connectivity, and subsurface structure; 2) physical properties – e.g., porosity, permeability, and resistivity; and 3) fluid presence, distribution, composition, and flux/flow rate. A method can (green) or cannot (red) be used to assess a given parameter. The traits of each method include: a) temporal applicability - whether the method can be applied at different times to observe temporal variability at the site; b) co-dependencies - whether input from another method is required for calibration and/or constraint; c) time and resource intensiveness - whether data can be produced with a given amount of resources on the timescale of weeks (low), months (medium) or greater than six months (high); and d) cost - a relative economic cost scale for completion (that can be qualitatively described as a method requiring desk time (low), laboratory time (medium) and/or ship time (high)).

Methods		Section	Method (Site) Parameters			Method traits		
			Fractures & structure	Physical properties	Fluids	Temporal applicability	Co-dependencies	Resource use
Acoustic (A)	Active acoustic	3.7	(red)	(green)	(green)	(green)	None	Low
Passive seismic (PS)	Passive seismic	3.6	(red)	(green)	(green)	(green)	None	Medium
Seismic reflection (SR)	2D seismic reflection	3.2.1-3.2.3	(green)	(red)	(green)	(red)	ST	Low-medium
	3D seismic reflection	3.2.1-3.2.3	(green)	(red)	(green)	(red)	ST	Medium
	4D/time-lapse seismic reflection	3.2.4	(green)	(red)	(green)	(green)	ST	Medium
Seismic tomography (ST)	Travel time tomography & FWI	3.3	(green)	(green)	(red)	(red)	SR	Medium-high
Seismic anisotropy (SA)	Shear wave splitting	3.4.1	(green)	(green)	(red)	(red)	SR, ST	High
	Seismic attenuation	3.4.2	(green)	(green)	(red)	(red)	SR, ST	High
	Ambient noise anisotropy	3.4.3	(green)	(red)	(red)	(red)	SR, ST	High
Controlled source electromagnetics (CSEM)	CSEM	3.5	(red)	(green)	(green)	(red)	SR	High
Direct sampling (DS)	Drilling & core analysis	3.8.1	(red)	(green)	(green)	(red)	SR	Medium
	Outcrop analogues	3.9	(green)	(green)	(red)	(red)	None	Low-medium
Laboratory experiments (LE)	Laboratory experiments	3.8.2	(green)	(green)	(green)	(red)	DS	Low
Modelling (M)	Numerical modelling	3.10	(green)	(green)	(green)	(green)	DS, SR	High
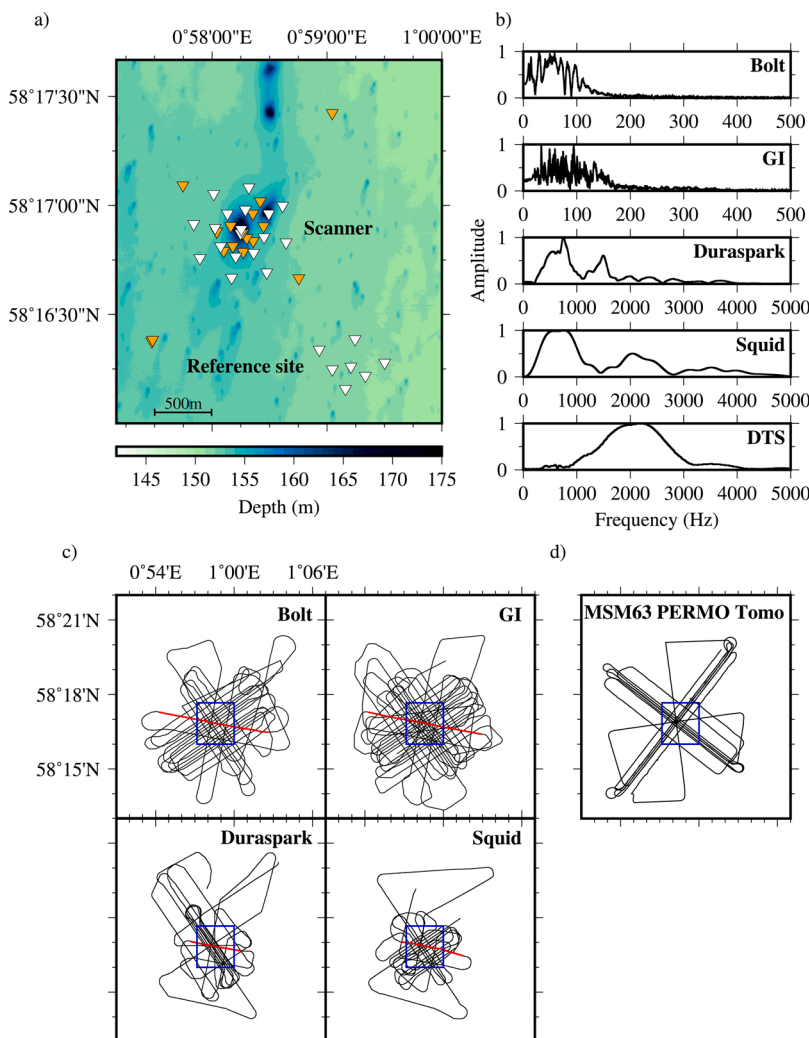
Fig. 3. Layout of the Scanner pockmark seismic experiments. a) OBS locations for JC152 seismic tomography, anisotropy, and passive seismic experiments (white triangles), and MSM63 seismic tomography experiment (orange triangles). b) Far-field source frequency spectra of the seismic sources used in the JC152 tomography and anisotropy experiments. c) Seismic acquisition tracks for JC152, with sources labelled, showing the multi-azimuthal geometry of source coverage. Only the airgun (Bolt and GI) and surface sparker (Duraspark and Squid) sources are shown. Blue box shows extent of area shown in a). Red line indicates location of the profiles shown in Fig. 4. d) Acquisition track for the MSM63 acquisition.
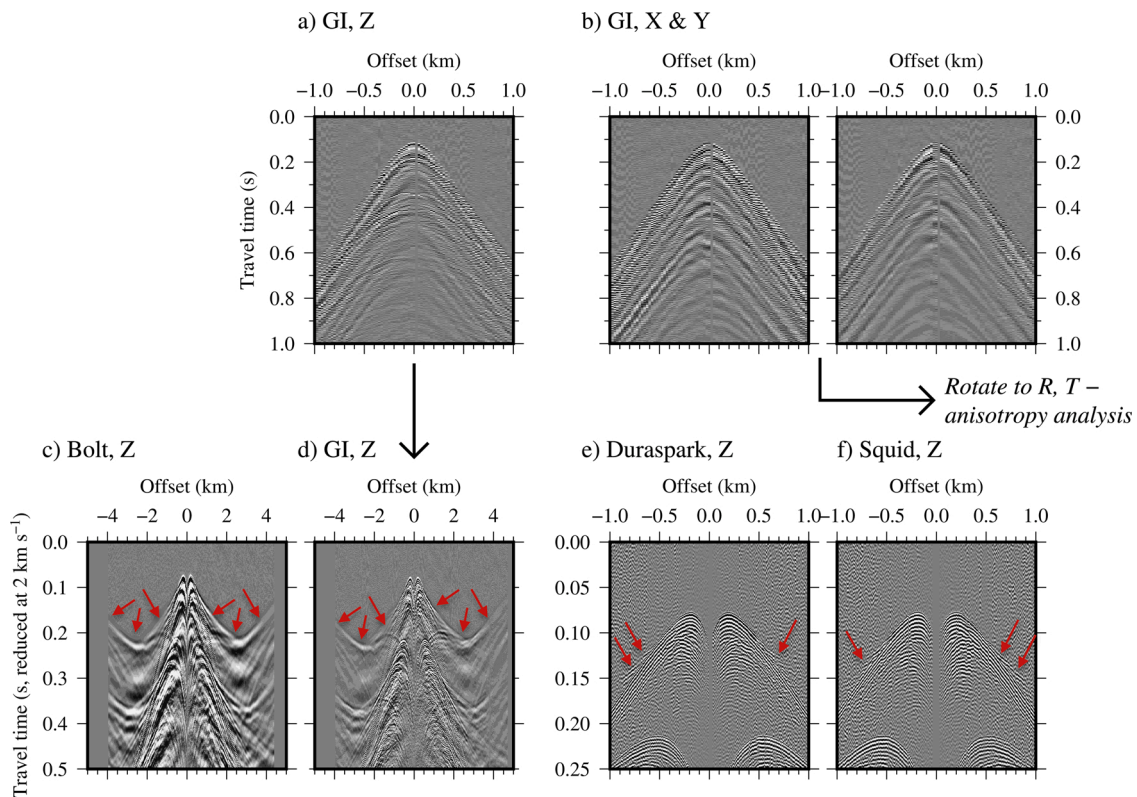
Fig. 4. Example OBS data from the JC152 seismic tomography and anisotropy experiments. All records shown are from OBS 1, located within Scanner pockmark, and are approximately E-W oriented (red lines, Fig. 3c). a) Z geophone component, GI source. b) X & Y geophone components, GI source, used for seismic anisotropy analysis. c)-f) Z component (c) Bolt, (d) GI, (e) Duraspark sparker, and (f) Squid sparker, plotted with reduction velocity of 2 km s^{-1}. Note the different horizontal and vertical scales for the airgun vs. sparker sources. Bolt and GI airgun records plotted with a 5-15 Hz low-pass filter. Sparker records plotted with a 100-200 Hz low-pass filter. Arrows show location of emergent (refracted) arrivals.

3.2.4. Time-lapse/4D seismic reflection

Time-lapse seismic imaging refers to the acquisition of seismic data at the same location at different points in time, in order to assess temporal changes in the subsurface. Where both seismic datasets are 3D, this may be referred to as 4D seismic imaging. This technique has been applied extensively to subsurface reservoir monitoring, including conventional and unconventional hydrocarbon production (e.g., Watts et al., 1996; Landrø et al., 1999; Barkved et al., 2003). Changes in the subsurface due to fluid flow may change properties such as fluid saturation, temperature, porosity, and pressure, and, hence, the elastic and stress-strain properties and behaviour of the rock, which cause a change in seismic response (Johnston, 2013). Such temporal changes can be used to better understand the formation and development of fluid flow features, as well as providing constraints for multiphase thermo-hydro-mechanical simulations. Recognising temporal changes in subsurface fluid flow systems is integral for monitoring CO$_2$ storage reservoirs and potential leakage in the overburden.

A principal challenge in time-lapse/4D seismic surveying is accounting for the repeatability, such that the produced images represent true temporal changes and not seismic artefacts associated with acquisition and/or processing. Attributes such as the normalised root-mean square noise are used to measure quantitatively the quality of the survey repeatability. Generally, repeatability is excellent where sediments are well stratified and undisturbed (e.g., Waage et al., 2019). However, since chimneys are often much more chaotic seismic structures, repeatability can be poor, and detection of changes in fluid flow between individual time-lapse surveys requires careful interpretation (Waage et al., 2019).

Time-lapse and/or 4D seismic data were not acquired at the Scanner pockmark complex. This technique has, however, been applied to the studies of actively-seeping chimneys, such as at Lomvi pockmark on the

Vestnesa Ridge, offshore W Svalbard (Bünz et al., 2012; Smith et al., 2014; Panieri et al., 2017), and for experimental fluid injections, including the Sleipner storage site (e.g., Arts et al., 2004; Chadwick et al., 2004, 2019; Boait et al., 2012; Eiken, 2019), the QICS experiment (Cevatoglu et al., 2015), and the STEMM-CCS Goldeneye release experiment (Flohr et al., 2021; Roche et al., in review). Time-lapse seismic data therefore play a key role in the understanding of both naturally occurring fluid flow, and CCS monitoring in pre-, active and post-CO$_2$ injection phases (Lumley, 2010).

3.3. Seismic tomography and full waveform inversion

The P- and S-wave velocity structure of a chimney and its surroundings can be determined by applying travel time tomography and full waveform seismic inversion. These techniques are applied with the principal aims of: locating gas-bearing zones; delineating the shape of the chimney; determining the presence and features of fractures (open or cemented, size and connectivity); and characterising the sediment properties within and outside the chimney.

Seismic travel time tomography is an inversion technique in which observed travel times (e.g., Fig. 4b) are compared to those computed through a discretised and parameterised model representation of the subsurface, with defined parameters that control the balance between minimising the data misfit and generating a model with the minimum required structure to fit the data. Travel time tomography approaches may be isotropic (e.g., Zelt and Barton, 1998) or anisotropic (e.g., Dunn et al., 2005), where in the latter the direction and magnitude of velocity anisotropy is fit and calculated directly, whereas in the former the anisotropy manifests as travel time residuals which can be analysed to determine the model anisotropic properties (Dunn and Toomey, 2001). Travel time tomography is a relatively low-resolution (normally
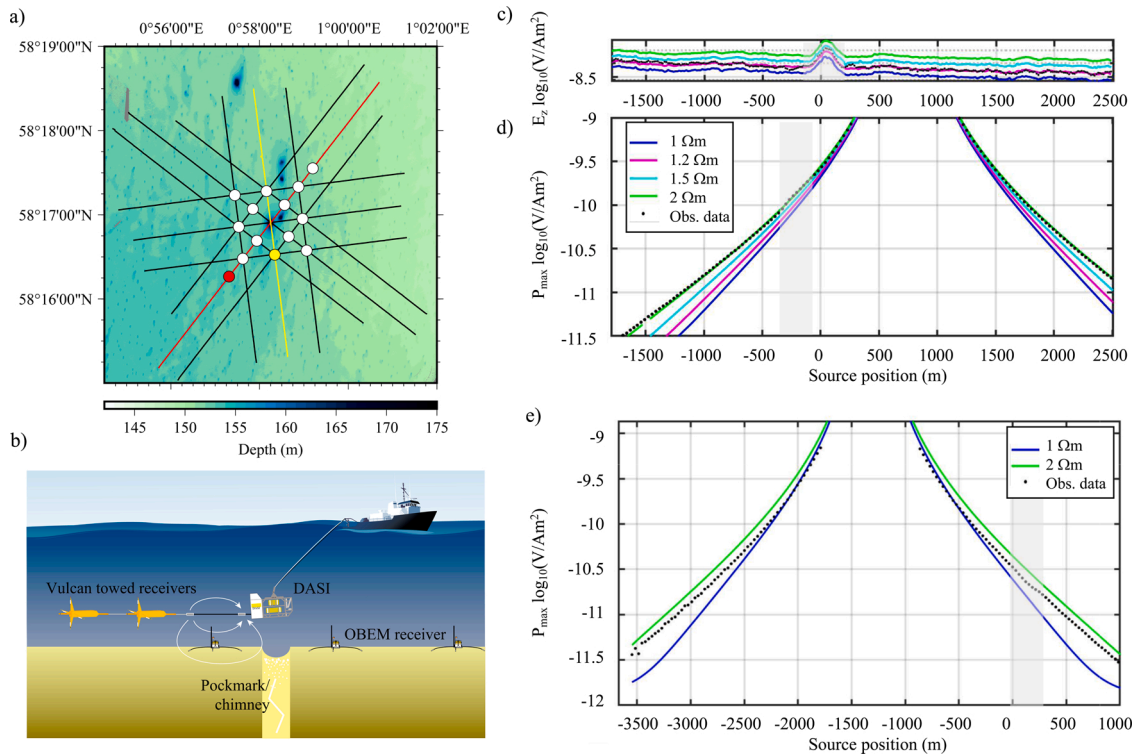
Fig. 5. Scanner pockmark CSEM experiment. a) Bathymetry map with data acquisition profiles (black) and OBEM receiver locations (circles). Data in c-e) are shown for profiles and OBEM instruments coloured in yellow (c-d) and red (e), respectively. b) Sketch of survey setup, with towed DASI source, towed Vulcan receivers and three component OBEM seafloor receivers. c-d) Example data at 1 Hz from N to S trending profile (yellow line) for the closest towed receiver c) and the OBEM d) (yellow circle on a). The x axis shows the source position (black antenna with white field lines in b)) along profile, with the location of Scanner pockmark set at 0 m. The OBEM in d) is located at ~700 m along profile. The observed data (black dots), the vertical electric field amplitude (E_z) and the total horizontal electric field amplitude (P_{max}) respectively, are compared to 2D (c), towed receiver) and 1D (d), OBEM) forward modelled data (coloured lines) for a subsurface with half-space resistivities of 1 to 2 Ωm. The towed receiver data, sensitive to the top ~50-100 m, agree well with predicted data for a 1.2 Ωm subsurface resistivity, while the OBEM data at larger offset to the source agree better with higher resistivities, indicating an increase in resistivity with depth. In c), the location of the grey box corresponds to observed E_z values when the transmitter is above the pockmark. In d), a slight increase of P_{max} at ~-200-400 m (highlighted with grey box), however, may indicate a localised increase of resistivities in the subsurface. e) OBEM instrument P_{max} data example from SW to NE trending profile (red line). At about 100-400 m from the Scanner pockmark position, a localised increase of P_{max} is observed, potentially related to an increase in resistivity in the subsurface in the vicinity of the seismic chimney.

hundreds of m to km laterally, hundreds of m vertically) imaging technique, with the resolution ultimately controlled by the shot and receiver spacings and further being dictated by the discretisation and parameterisation of the model.

The final OBS tomography model can be used as the initial model for full waveform inversion of OBS data (FWI; e.g., Virieux and Operto, 2009). FWI uses the entire recorded seismograms, and, therefore, includes amplitude and phase information instead of solely using the travel times. As a result, FWI represents a higher resolution technique, which is now widely used in crustal-tectonic (e.g., Morgan et al., 2013; Górszczyk et al., 2017; Davy et al., 2018) and engineering (e.g., Smithyman et al., 2009) contexts, in addition to being widely adopted across the hydrocarbon sector (e.g., Sirgue et al., 2010; Prieux et al., 2013). The effectiveness of FWI is highly sensitive to the starting model being capable of predicting the travel time within half a dominant period, in order to avoid cycle-skipping (Virieux and Operto, 2009). This approach is, therefore, commonly preceded by travel time tomography.

Two phases of data acquisition (Fig. 3a) were conducted at the Scanner pockmark complex to acquire data suitable for the application of first arrival seismic travel time tomography and full waveform inversion. The first survey, conducted during cruise MSM63, utilised an array of 18 OBSs, with shots generated using two GI airguns. The OBS and profile locations are shown in Fig. 3a & d respectively. A second, more extensive experiment was conducted during cruise JC152, coincident with the anisotropy experiment (described in section 2.4, below), and utilising an array of 18 OBSs located in and around Scanner

pockmark and 7 at a nearby reference site, located ~1 km southeast of the pockmark, where industry 3D seismic data showed no evidence of the presence of gas (Fig. 3a). These instruments recorded shots from all of the seismic sources used in the experiment (Fig. 3c). Fig. 4c-f shows the shots recorded on an OBS located within Scanner pockmark for an ~E–W oriented profile for each of the airgun and surface sparker sources.

While travel time tomography approaches are not necessarily reliant on a priori information, it is important to consider additional constraints, where available, since a poorly constrained inversion may produce a biased result, based on its parameterisation and/or starting model (Zelt et al., 2003). Interpreted multi-channel seismic profiles may be used to inform the initial P-wave velocity model. In turn, the results of travel time tomographic modelling can be employed to improve the processing and interpretation of multi-channel seismic profiles, by providing independent velocity information. The wider-angle transmission regime involved in OBS methods also assists in resolving the issue of acoustic blanking beneath gas accumulations, such as those observed beneath Scanner pockmark (Fig. 2c), and provides a further tool for the verification of whether observed chimneys represent actual subsurface geological features, or reflection imaging artefacts.

The two seismic approaches, multi-channel seismic reflection imaging and tomography, are highly complementary to one another and may be utilised most effectively when applied synchronously. The results of seismic tomography are also complementary to laboratory scale rock physics experiments, since they place constraints on larger scale in situ

physical properties, and, thus, fracture orientations and fracture density (Amalokwu et al., 2017; Jin et al., 2018), which then can be used to complement the geo-mechanical models.

3.4. Seismic anisotropy

Fractures in sedimentary settings play a crucial role in defining the physical properties of subsurface reservoirs, as they enhance porosity and permeability, or conversely may contribute to reservoir compartmentalisation. Thus, fracture orientation, size, volumetric density, and connectivity are of interest to the understanding of subsurface fluid flow. Attribute analysis of stacked seismic images, which includes techniques such as coherence analysis (e.g., Bahorich and Farmer, 1995), can detect larger fractures. However, these techniques are unable to image smaller fractures, below the spatial resolution of the seismic image. Therefore, in order to determine fracture properties at sub-seismic scale, seismic anisotropy analysis can be applied, which utilises the directional dependence of transmitted seismic signals. A range of theories have been developed to describe the elastic response of fractured rocks (e.g., Hudson, 1981; Thomsen, 1995). While these theories generally agree for dry rock, they differ considerably where fluids and fluid flow between cracks and pores are present (Liu et al., 2000).

Estimating fracture sizes from narrow-band observations of seismic anisotropy may lead to misinterpretations, as there is an ambiguity whereby a medium containing a small number of large fractures will generate the same response as a medium containing a larger number of smaller fractures (e.g., Maultzsch et al., 2003). Therefore, a frequency-dependent approach to studying anisotropy, which is sensitive to the length-scale of the causative mechanism for the anisotropy, is required. Properties such as fracture scale length and fluid saturation can then be inferred from the frequency-dependence of anisotropic attributes, as predicted by theoretical work (Chapman, 2003; Jakobsen and Chapman, 2009). The impact of partial saturation on anisotropy and attenuation in materials of known fracture density and orientation has been studied using models that can link laboratory and field datasets (Amalokwu, 2016), which are required to make robust determinations of permeability.

The Scanner pockmark anisotropy experiment used several seismic sources with different frequencies, in the range ∼10 Hz to 2 kHz, as described above (Fig. 3b). This broadband dataset was specifically designed for the measurement of frequency-dependent anisotropy, to permit enhanced fracture characterisation. In order to achieve maximal azimuthal coverage, which is necessary for determining the directionality of anisotropy, profiles were acquired at multiple orientations through the OBS array (Fig. 3c). Several approaches are available for investigation of frequency-dependent anisotropy associated with chimneys. Details of the two active source and one passive source methods that were used at Scanner pockmark are provided below.

3.4.1. Shear-wave splitting

The measurement of seismic travel time anisotropy using shear-wave splitting (SWS) is an established technique for determining the orientation and density of fracture networks (e.g., Crampin, 1985). Shear-wave splitting occurs when a polarised shear wave enters an anisotropic medium. When this occurs, the shear wave is split into two orthogonal components, oriented perpendicular and parallel to the fracture normal direction. The two split shear waves travel at different speeds through the fractured medium, resulting in differences in their travel time. SWS analysis uses converted P-to-S waves to determine the orientation of a symmetry axis associated with the fracture normal direction. SWS distinguishes between different anisotropic symmetry systems, which produce characteristic patterns that can be observed in transformed radial and transverse components of the horizontal geophone records (Fig. 4b). This approach can be used to differentiate between dominant horizontal transverse isotropy, which may be associated with vertically aligned fractures, and vertical transverse isotropy,

which may arise in the presence of concentric fractures.

The orientation of these symmetry planes and the directions of the fast and slow S-wave arrivals can be used to determine the fracture orientations. The measured delay between the fast and slow S-wave arrivals is used to determine the intensity of anisotropy, which is related to the fracture size and/or density (e.g., Crampin, 1985; Mueller, 1992; Li, 1997). Raw estimates of SWS give only depth-averaged estimates of fracture properties. Therefore, to determine the depth variation of both fracture orientation and density, a layer-stripping approach is required (Haacke et al., 2009), which recursively compensates and removes the anisotropy measured in shallow layers. Shear-wave splitting analysis is applied to the study of the chimney beneath Scanner pockmark in order to map the geometry and extent of the fracture network. This approach allows us to distinguish between different hypotheses for the structure of chimneys.

3.4.2. Seismic attenuation

While S-wave velocity anisotropy, observed through SWS analysis, is sensitive to both open and closed fracture networks, attenuation anisotropy is primarily sensitive to open fracture networks and the fluids that may be present within these (e.g., Worthington and Hudson, 2000; Chapman, 2009). Attenuation may occur through mechanisms including scattering and wave-induced fluid flow (Baird et al., 2013). Scattering of seismic waves due to aligned heterogeneities has long been recognised to be frequency dependent (e.g., Shapiro and Hubral, 1995; Werner and Shapiro, 1999).

Field observations of attenuation anisotropy have been reported from walkaround vertical seismic profile data (Varela et al., 2006; Maultzsch et al., 2007; Bouchaala et al., 2019), with the observed effects often being consistent with the predictions of poroelastic models accounting for wave-induced fluid flow (Chapman, 2003). If wave-induced fluid flow is the dominant mechanism for the observed attenuation anisotropy, then the phenomenon may provide a link to fracture induced permeability. Chapman (2009) considered the case of multiple sets of fractures having different fluid connectivity.

Application of seismic attenuation and attenuation anisotropy analysis at Scanner pockmark was directed at investigating both the geometry (cf. SWS) and contents of subsurface fracture networks, where these are present. As with travel time anisotropy, the broad-band frequency nature of the various seismic sources used is required to discriminate between the properties of fractures of different sizes, which may otherwise not be distinguished.

3.4.3. Ambient noise anisotropy

Methods for analysing surface waves from ambient noise utilise lower frequencies, typically <1−2 Hz, than the active seismic sources. This approach further extends the frequency range of frequency-dependent analyses to determine fracture properties. Rayleigh wave velocities can be measured on the vertical and hydrophone components of the OBS. By taking spectrograms of cross-correlations between OBS pairs (processed according to Bensen et al., 2007) located on opposite sides of the chimney, Rayleigh wave phase-velocity dispersion can be measured (Yao et al., 2006) and used to invert for vertical shear-wave velocity structure. Applying Radon transforms to a set of cross-correlations between all possible OBS pairs within an array and summing these over time, a technique known as 2D beamforming (Lacoss et al., 1969), shows the slowness at which Rayleigh waves cross the array at all azimuths. This method facilitates full-azimuth observations of anisotropy (Alvizuri and Tanimoto, 2011).

However, there are limitations on the frequencies that can be observed using passive methods, which arise due to the OBS array geometry. The largest spacings within the array, termed the aperture, used at Scanner pockmark result in a lowest usable frequency of ∼0.5 Hz (Rost and Thomas, 2009). For beamforming there are also challenges arising from the array geometry. While the OBS array located at the Scanner pockmark is relatively symmetrical, the array at the reference

site is not, and so has a highly asymmetric response in the slowness domain, which causes aliasing effects that can cause artificial anisotropy to be observed. For analysis of azimuthal dependence to be effective, any artificial anisotropy must be removed (Picozzi et al., 2010).

Cross-correlation analysis and 2D beamforming can be used to observe the dispersion and azimuthal dependence of Rayleigh waves and can be inverted for 1D shear wave velocity structure at Scanner pockmark in the 0.5–1.5 Hz range. This technique contributes both to constraining the structure of the chimney and extending the range of frequencies which can be used for considering frequency-dependent anisotropy characteristics.

3.5. Controlled source electromagnetic surveying

The marine controlled source electromagnetic (CSEM) method is used for mapping variations in the electrical resistivity of the subsurface (e.g., Cheeseman et al., 1987; Edwards, 2005). The CSEM method used in this study involves towing a horizontal electric dipole close to the seabed that transmits an alternating electromagnetic field. The electromagnetic energy diffuses through the seawater and seafloor and is recorded by electric field receivers that are towed in-line behind the transmitter and others that are stationary on the seafloor (Constable, 2013). The measured field amplitude and phase lag between source and receivers relate to the electrical resistivity of the seafloor. When more resistive Earth materials are encountered (e.g., low porosity sediments), elevated electric fields are observed at the receivers and the phase lag is reduced.

The CSEM method is sensitive to changes in the bulk electric resistivity structure of the Earth, a property that depends on lithology and mineral composition but is particularly sensitive to connected porosity and pore fluid content (Palacky, 1988). Due to this sensitivity to sediment pore fluids, the marine CSEM method has been widely used for hydrocarbon exploration (e.g., Ellingsrud et al., 2002; Constable, 2010). Electrical resistivity is also an indicator for whether pathways for fluids to the seabed exist, as the presence of aligned permeable and conductive fractures may lead to electrical anisotropy (e.g., Naif et al., 2015).

The CSEM survey at Scanner pockmark was conducted during cruise MSM63, using the University of Southampton deep-towed active source instrument (DASI; Sinha et al., 1990), towed at $20-40$ m above the seafloor. The source signal comprised a ~100 A, 1 Hz square wave. Twelve profiles were acquired, oriented in four different azimuths to assess the electrical anisotropy. Two different types of receiver were utilised to record the induced field: an array of 14 ocean bottom electromagnetic (OBEM) field receivers (6 three-component receivers and 8 horizontal-component receivers; Fig. 5a), here measuring the electric field only, and two three-axis Vulcan electric field receivers towed behind the source (Fig. 5b; Constable et al., 2016). The CSEM data from both receiver types are processed with a Fourier transform over 1 s-long windows to obtain amplitude and phase data in the frequency domain, and stacked over 60 s-long windows to improve the signal-to-noise ratio (Myer et al., 2011). Estimating the electrical resistivity distribution from the data requires the use of modelling procedures. For the towed receivers (Fig. 5c), 2D forward modelling for a homogeneous subsurface with one resistivity value (half-space) is performed to compare the modelled data to the observed vertical electric field amplitude (E_z) data and estimate the subsurface resistivity. For the seafloor receivers (Fig. 5d,e), the magnitude of the major axis of the polarisation ellipse traced by the electric field, P_{max}, is compared to 1D forward modelling results for half-space resistivities. P_{max} is independent of the receiver orientation. Resistivities appear to increase with depth. Inversion algorithms (e.g., Constable et al., 1987) which optimise the fit between the observed and predicted data are required to estimate a heterogeneous resistivity structure (analysis for the towed receivers is presented in Gehrmann et al., in review).

There are trade-offs between the thickness and resistivity of anomalous features (e.g., Edwards, 1997) that can be overcome using prior geological knowledge or constraints from complementary data. For example, seismic reflection data can provide high resolution imaging of geological stratigraphy and structures, while CSEM is able to detect the presence and type of fluids in the pore space, such as hydrocarbons, CO_2, and variations in salinity. The difference between changes in pore fluid or lithological variations may be distinguished by interpreting CSEM and seismic data in conjunction (e.g., Hoversten et al., 2006). Geological interpretations benefit from combined analysis with, for example, wide-angle seismic data (e.g., Goswami et al., 2015), seismic reflection data (e.g., Weitemeyer et al., 2011; Attias et al., 2016; Berndt et al., 2019), magnetic data (Gehrmann et al., 2019), and well logs (e.g., Harris et al., 2009).

The CSEM method is, overall, a relatively low-resolution method ($10-1000$ m), due to the diffusive nature of EM fields. The specific resolution and penetration depth depend on the source-receiver geometry, the number of receivers at different offsets to the source, and the frequency spectrum of the source signal (Edwards, 1988). The dual-receiver approach used here includes towed instruments sensitive to the shallow subsurface and OBEM receivers sensitive to the deeper subsurface. For the purposes of understanding potential subsurface fluid escape structures, the CSEM method provides a tool to map variations in resistivity related to connected porosity and fluid/gas content of seafloor sediments.

3.6. Passive seismic methods

Passive seismic monitoring involves the use of seismometers and sound recording devices, such as OBSs, located at the seafloor. These instruments provide continuous recordings, and, therefore, capture events during seismic acquisition interludes. In the Scanner pockmark seismic experiment, passive seismicity was recorded using the same OBS array as for the anisotropy experiment (Fig. 3a).

Various types of events were detected using this approach, including: short (<1 s) duration events, similar to those previously detected in gas seepage areas (Tary et al., 2012; Bayrakci et al., 2014; Batsi et al., 2019), and which may represent collapses and/or the formation of small pockmarks; medium (few seconds) duration events, comparable to a volcano-tectonic tremor (e.g., Latter, 1981; Harrington and Brodsky, 2007), rarely observed in this tectonic context, and which may represent the movements of fluids in conduits in the shallow subsurface; and events related to bubbles escaping at the seafloor. The low frequency content displayed by these types of events (<30 Hz) means it may also be possible to identify these events during periods of, for example, sparker seismic acquisition, due to the much higher frequency content of the source signal (≥200 Hz).

For recorded seismicity associated with gas bubble escape at the seafloor, the Minnaert (1933) equation can used to estimate the bubbles' radii from the frequencies of the events. However, this approach may not be able to distinguish between the acoustic signature of many small bubbles and one big bubble, which highlights the necessity to calibrate this approach using additional methods (e.g., active acoustics).

Passive monitoring of seismicity associated with methane venting and/or fluid movement in the subsurface at Scanner pockmark aims to quantify the gas flux through the chimney to the seabed and into the water column. Unlike active acoustic methods, this approach represents a continuous monitoring tool. The microseismic events detected through passive monitoring may be associated with the local tidal cycle and, hence, may indicate a possible correlation between tides and the movement of fluids from a subsurface reservoir to the seabed. Furthermore, if the seismicity is a result of fluid movement at depth, it may be applicable to studies of fluid flow beneath the cap rock or overburden, where the fluids do not directly reach the seabed.

3.7. Active acoustic methods

Hydro-acoustic surveying involves the use of either single- or multi-

beam echosounders, which transmit one or more beams, respectively, of monochromatic frequency beneath the ship. The delay associated with the returning pulse is typically used to map the underlying bathymetry, while the strength or amplitude of the returning pulse can provide information on the physical properties of the reflecting medium. Given the strong impedance contrast between water and gas, hydro-acoustic methods are sensitive to the presence of gas bubbles in the water column (Fig. 6). The gas bubbles rise due to buoyancy, drawing surrounding fluid into and upwards with the plume, with lateral dispersion as a function of bubble rising velocity and water current velocity. The gas plume comprises bubbles of various sizes, with larger bubbles possessing relatively higher rising velocity and smaller bubbles possessing relatively lower rising velocity. The plume can be observed to rise to the thermocline at ~40 m below sea surface (Fig. 6; Böttner et al., 2019; Li et al., 2020).

Multi-beam data can be used to map the three-dimensional extent of gas plumes escaping from pockmarks and, across multiple surveys, observe variations over time. Seabed currents may cause the plume to separate based on differing bubble size distributions, which can be mapped using multi-beam data (Li et al., 2020). Similarly, observing the target strength of gas plumes in single-beam data can be used to estimate the bubble size distribution and gas flux being released from the pockmark, provided a range of frequencies covering the bubble resonance frequency are used (Li et al., 2020).

Active hydro-acoustic surveying was applied in the study of the active venting at the Scanner pockmark in order to quantify the gas flux from the seabed and to study the gas plume evolution in the water column. Repeat surveys can also be used to determine if there is any temporal variation, for example due to tidal cycles (e.g., Boles et al., 2001; Schneider von Deimling et al., 2010). Temporal patterns may also be compared with observations from passive seismics, which provide a continuous record of gas venting at the seabed, or of the migration of fluids at depth.

3.8. Direct sampling of sediments and pore fluids

3.8.1. Drilling and coring

Direct sampling of seabed sediments via coring allows for a local characterisation of lithology, porosity, and other geophysical and geochemical attributes at centimetre-scale or less resolution, providing a verification of geophysical properties and parameterisation for numerical models. Detailed description of sediments in terms of their lithology, physical, and chemical properties allows determination of the geological origin of the sediments, the extent and characteristics of specific stratigraphic units, the possible origin of the pore fluids, and a very high-

resolution, visual observation of changes in sediment texture and fabric. Changes in sediment colour, e.g., the presence of black layers that form when methane is consumed by anaerobic methane oxidation with sulphate, and the structure of the sediment, e.g., the presence of outgassing and fluidisation structures, provide evidence for the presence of gas in the sediment, as well as evidence for palaeo-fluid migration. Further, non-invasive 3D analysis of sediment structure is possible using XCT imaging techniques (Fig. 7b–e), which can highlight the spatial distribution of dense materials such as iron sulphides that can form during anaerobic methane oxidation (Fig. 7c,e). Geochemical analyses of pore fluids can be used to determine their origin and, hence, the presence of migration pathways and the connectivity of different layers. Geochemical analyses of the solid phase allow understanding of the chemical reactions that are occurring or have occurred in the sediments and can explain physical properties, such as changes in permeability caused by carbonate or iron sulphide precipitation. Methane derived authigenic carbonates in the sediments and on the seafloor are indicators for prolonged presence of fluid flow, and can be dated to derive information about fluid flow history.

Sediment cores from the Scanner pockmark complex and a reference site located ~7 km to the east (Fig. 1b,c) were recovered using the BGS Rockdrill (RD2) and a gravity corer during cruises MSM78 and POS518-2 (Fig. 7b). RD2 is a remotely operated multi-barrel wireline subsea robotic sampling system that continuously cores 1.72 m-long sections, with a diameter of 6.1 cm. The maximum drilling depth was 33 mbsf at the reference site. Gravity cores were collected from the uppermost 5.75 m of the sediment column using a 12.5 cm-diameter tube driven into the seabed under weight-assisted free-fall (Linke and Haeckel, 2018).

Immediately following collection of the sediment cores, pore waters and sediment samples were extracted from both RD2 and gravity cores. Pore waters were collected with 0.2 μm-pore diameter Rhizons (Seeberg-Elverfeldt et al., 2005; Dickens et al., 2007) at approximately 30 cm depth intervals, and preserved for analyses of cations (e.g., dissolved Ca, Fe, Mn, Si, B), anions (e.g., Cl, SO_4, total alkalinity), nutrients (NH_4, PO_4, Si, NO_x), and dissolved sulphides. Samples of the sediments were collected with cut-off 5 cm syringes and analysed for their methane concentrations and methane carbon isotopic composition, porosity, grain size, and organic and inorganic carbon content. The cores were then scanned using a GEOTEK multi-sensor core logger (MSCL; Fig. 7a), to measure acoustic wave velocity, density, resistivity, and magnetic susceptibility, before being sectioned horizontally, photographed, and logged. The chemostratigraphy of the sediment was then measured in high resolution (1 mm) with the ITRAX XRF core scanner.

Some caution is required during core logging and interpretation, as artefacts such as small-scale fractures and other disturbances can be
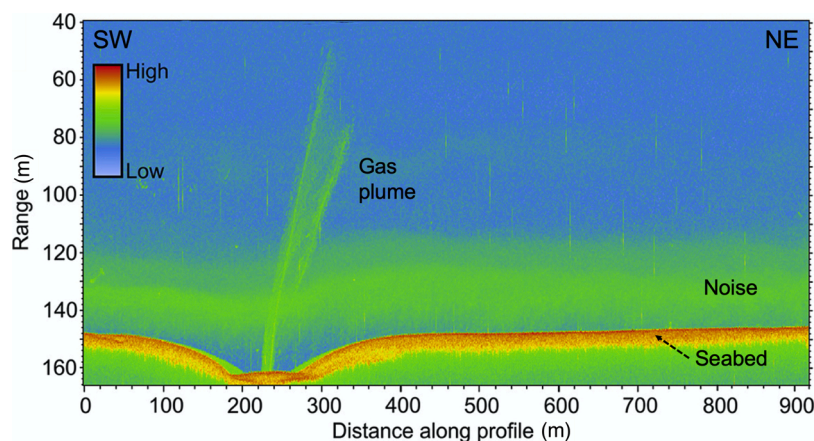

Fig. 6. Hydro-acoustic imaging of the Scanner pockmark gas plume, using EM712 echosounder data at a frequency range of 40-100 kHz. Highest backscatter is displayed in red (seabed). The gas plume is clearly visible as a strong (green) zone of backscatter emanating from the pockmark, rising to the thermocline at ~40 m below the sea surface. Figure adapted from Böttner et al. (2019).
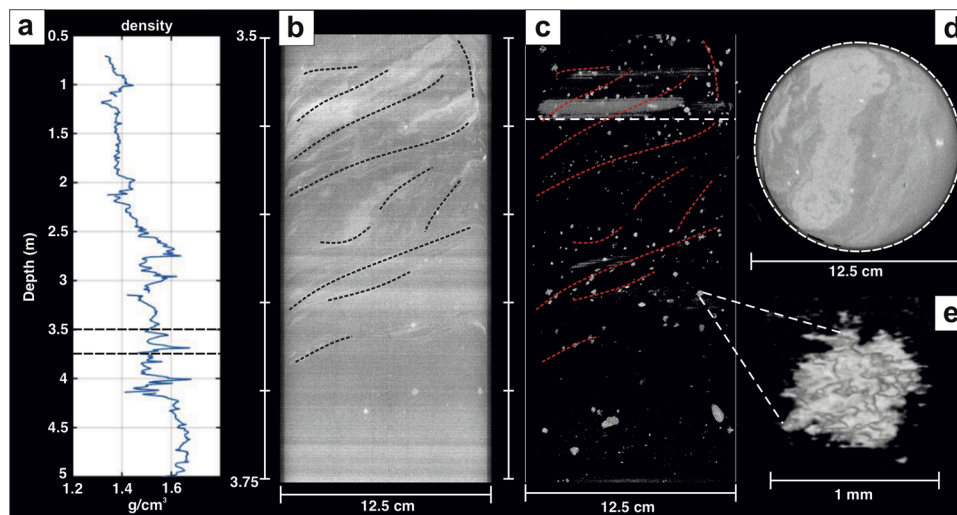
Fig. 7. Gravity cores of sediments recovered from directly beneath East Scanner Pockmark (GC17; Fig. 1c) during the MSM78 expedition. The cores were analysed using a) Multi-Sensor Core Logging (MSCL), which includes density data and b-e) X-ray micro-CT analysis. b) and d) Analysis of a 25 cm length x 12.5 cm diameter core section composed of fine silt. Coarser grained horizons (lighter grey) show evidence of fluidisation structures and layering, picked out by the dotted lines. c) Same image as b) but with lower density material removed, showing the presence of disseminated iron sulphide (bright spots, close-up shown in e) that has precipitated within the coarser grained horizons. The presence of iron sulphide is indicative of transport of methane-rich fluids through the coarser grained sediment horizons.

introduced during the drilling procedure. This is particularly important for soft, non-lithified sediments such as those found in our study area, as the coring process may reduce porosity, due to dewatering compaction and shear straining (Bouma and Boerma, 1968; Blomqvist, 1985). Concentrations of some reactive geochemical parameters (e.g., dissolved Fe, dissolved inorganic carbon, H_2S and CH_4) may further be affected by outgassing or chemical oxidation during the retrieval and subsampling of the cores. These effects can be minimised by subsampling immediately after core recovery, or by the use of in-situ measurement techniques such as lab-on-chip sensors (e.g., Whitesides, 2006).

While coring and drilling approaches allow very high (cm-scale) vertical resolution, the horizontal resolution is limited by the number of sediment cores that can be taken within the time frame of an expedition. Therefore, appropriate sampling strategies are required to effectively integrate the information from sediment cores with information gathered using other approaches. For the purpose of our study, previously acquired seismic, real-time fast-track processed seismic lines, and prior information about the shallow geology were used to inform our drilling strategy. However, at the Scanner pockmark drilling locations, RD2 settings were configured for recovery of authigenic carbonates, rather than unconsolidated sediments, and, as a result, sediment recovery was rather low (~50 %), due to washout of loosely consolidated sand intervals.

The integration of sediment core and geophysical data maximises their inherent value, by providing localised sub-seismic resolution site-specific constraints (Vardy, 2015; Vardy et al., 2017; Provenzano et al., 2018). Multi-sensor core logging of sediment cores permits the measurement of geophysical and geotechnical parameters, providing a way to: calibrate the two-way-time seismic reflection data to depth; constrain seismic inversion and interpretation within a range of plausible values (e.g., Provenzano et al., 2018); interpret and cross-validate the results of seismic tomography and CSEM methods; and interpret physical properties in terms of changes in sediment properties, such as porosity (e.g., Vardy, 2015; Baasch et al., 2017). Appropriate calibration of the instruments is necessary for a meaningful comparison between samples acquired using different coring techniques and core liner materials, and the need to account for laboratory temperature and humidity conditions.

3.8.2. Geomechanical testing and sediment core analysis

Rock physics experiments permit the direct examination of the changes in geophysical, geomechanical, and geochemical sample properties under controlled conditions in the laboratory. Two rock physics experimental setups were used in combination for the study of coupled thermo-hydro-mechano-chemical phenomena occurring in a rock-brine-

CO_2 system: (1) multi-flow CCS and (2) acoustic pulse tube rigs.

Firstly, the multi-flow CCS rig permits the analysis of geophysical signatures (ultrasonic P- and S-wave attributes, and electrical resistivity) of reservoir rocks subjected to brine and CO_2 flow-through tests at controlled reservoir pressure and temperature conditions, resulting from the hydromechanical changes occurring in the rock sample due to CO_2–brine fluid substitution effects and rock-fluid reactivity. Secondly, the acoustic pulse tube rig allows the measurement of seismic velocity and attenuation of P-waves in sediment and rock samples over a frequency range of $1-10$ kHz and S-waves at 500 Hz. This frequency band complements the ultrasonic frequencies obtained by the multi-flow CCS rig and helps to constrain improved rock physics models accounting for fluid mobility and frequency-dependent seismic effects (Batzle et al., 2006; Mavko et al., 2009). In addition, the P- and S-wave frequency ranges of the acoustic pulse tube measurements partially overlap with the sparker sources used for the seismic anisotropy assessment of the Scanner pockmark (Fig. 3b), permitting the calibration of the seismic data under controlled conditions in the laboratory.

The experimental approach used provides a geophysical and hydromechanical assessment of fluid flow in (i) CO_2 reservoir rocks and (ii) the shallowest section of the marine sediment overburden. In the former case, the reservoir rock experiments simulate variable spatial-temporal states during (drainage) and post- (imbibition) CO_2 injection, considering homogeneous (background) and fractured (slip-related features) reservoir samples. In the latter case, the tests focus on the hydrodynamic response of near-seabed sediments subjected to variable CO_2 flow rates.

A study of reservoir rocks was conducted using natural reservoir samples (Utsira sand formation, Sleipner; Falcon-Suarez et al., 2018), and quartzose synthetic sandstones manufactured in the lab following the procedure described in Falcon-Suarez et al. (2019), including homogeneous (Falcon-Suarez et al., 2016, 2017) and fractured samples (Muñoz-Ibáñez et al., 2019). In all tests, an increasing CO_2-to-brine partial flow condition was imposed through the originally brine-saturated samples, in order to progressively saturate the sample in CO_2. The confining stress, pore pressure, and temperature conditions slightly varied between tests, within the ranges $16-40$ MPa, $7-12$ MPa, and $20-35$ °C, respectively. The fluid substitution process and related hydromechanical response of the rock were assessed though the continuous monitoring of ultrasonic P- and S-wave velocity and attenuation, electrical resistivity, axial and radial strains, and hydraulic conductivity.

Fig. 9 shows a comparison between the results obtained using a synthetic (Falcon-Suarez et al., 2016) and a natural (Falcon-Suarez et al., 2018) sandstone, with similar composition and porosity. The arrival of CO_2 in the rock samples lead to increased resistivity, together with a

sudden drop (>5%) in P-wave velocity and increase in the attenuation (more significant in the synthetic sample), while subsequently increasing the CO_2 content had only limited further effects. Forced imbibition is used to study the trapping efficiency of the rock through evaluation of the residual CO_2 content and the geophysical signatures associated with this value. In this regard, Muñoz-Ibáñez et al. (2019) studied the hydrodynamic behaviour of a fractured reservoir analogue sample, and found that non-connected fractures may act as larger cavities than background porosity, and these cavities are energetically favourable for CO_2 storage. Therefore, non-connected fractures have the potential to enhance CO_2 trapping and the overall sealing efficiency of CO_2 storage reservoirs (Muñoz-Ibáñez et al., 2019), in contrast to the role played by a connected fracture network (i.e., the hypothesised structure of a chimney).

In addition, gravity core samples from cruise POS527 (Achterberg and Esposito, 2018) were used to conduct flow-through experiments, to analyse the coupled hydro-mechanical-chemical response of seafloor sediments subjected to sudden gas release episodes (e.g., pockmarks). These experiments included (i) a set of permeability tests to monitor the sediment reactivity to CO_2 (i.e. dissolution/precipitation), and (ii) a simulation of the STEMM-CCS CO_2 release experiment (Flohr et al., 2021) to collect linked geophysical-hydromechanical information about the target site under controlled conditions in the laboratory. The data collected during these experiments indicate permeabilities of $\sim 10^{-16}\,\mathrm{m}^2$ in the upper part of the sediment column. Preliminary analyses of reactive transport models (Marín-Moreno et al., 2019) indicate that the sediment is largely unreactive to the exposure of CO_2 saturated brine, while the grain size may be conditioning the CO_2 distribution within the sediment; from clay- to sand-rich layers the distribution becomes more homogeneous (Roche et al., in review).

For further understanding of hydraulic fracturing and gas migration mechanisms, flow-through experiments were carried out on gravity core samples recovered from locations adjacent to the STEMM-CCS CO_2 release site during the RV Poseidon cruise POS534 (Schmidt, 2019). Combining geomechanical testing with XCT imaging (Fig. 10d; Deusner et al., 2016) allows the visualisation of fracture formation in response to pressure accumulation and fluid injection. Fracture formation in the poorly consolidated clay sediments started at a low critical pressure of $\sim 5 - 15$ kPa above the confining stress (Fig. 10a). Fracture propagation was essentially perpendicular to the major principal stress direction, likely resulting from the formation of disk-shaped gas bubbles with high aspect ratios, as expected in clay sediments (Boudreau et al., 2005). Fracture formation was first observed from rapid gas pressure dissipation (Fig. 10b, event 4) and the appearance of a small gas accumulation in the XCT image projections (Fig. 10c). Mass balancing of the injected gas and changes in confining volumes after fracture opening until the end of the first injection interval indicate a high apparent fracture permeability (Fig. 10b). Flow-through experiments and coupled thermo-hydro-chemo-mechanical studies can provide important insight into fracture formation and propagation in natural sediments, and are an important tool to develop and validate numerical models of chimney evolution. However, mechanical and hydraulic constraints in small-scale laboratory experiments will not provide an exact replication of the in-situ field environment, which must be carefully considered during experimental planning and data interpretation.

3.9. Onshore outcrop analogues

In addition to direct sampling of an actively venting system, further characterisation and the long-term development of fluid escape structures can be determined from analysis of onshore outcrop analogue systems. Field outcrops permit characterisation of physical structure, geometry, and physical properties, and understanding of past physical, chemical, and hydro-mechanical processes, through direct observation and sampling. However, fluid escape outcrop analogues are challenging features for comparative analysis with active subsurface systems (e.g.,

Roberts et al., 2017). Following the cessation of active fluid flow, a number of diagenetic and surface processes may alter the physical properties of the rocks, which can include post-dewatering compaction, cementation, groundwater-induced geochemical alteration, weathering, and erosion. XCT techniques can be utilised to acquire 3D digital rock images of the outcrop samples, whereby the cement can be selectively removed using image processing techniques, allowing the study of the physical and hydraulic properties of the rock formation prior to cementation (Fig. 8d; e.g.. Böttner et al., in review).

There is often a discrepancy between the scales of fluid flow features observed in onshore outcrops and their seismic manifestations, whereby chimneys observed in seismic data can extend several hundreds of metres in diameter and up to 1000 m in height (Berndt, 2005; Cartwright et al., 2007; Løseth et al., 2009; Andresen, 2012; Karstens and Berndt, 2015). Outcrops of sand-filled fractures in California (Fig. 8c), which are sand intrusions that form due to exceedance of lithostatic pressure and subsequent remobilisation and fluidisation of sediments (Huuse et al., 2010; Hurst et al., 2011), have been observed to reach similar dimensions to their corresponding seismic discernible features (Huuse et al., 2005; Ross et al., 2014). However, the largest known field outcrops of hydrocarbon-derived carbonate conduits, located in Varna, Bulgaria, are only up to 10 m high and ~ 1 m in diameter, and are spread over a comparatively small area ($2.4 \times 10^5\,\mathrm{m}^2$; De Boever et al., 2006a, 2006b). The lack of outcrop evidence for fracture systems that extend up to 1000 m in vertical height and with large spatial extent is likely a consequence of the preferential preservation of hard parts, as suggested by the observed sand-filled fractures and carbonate pipes in California and Varna respectively (De Boever et al., 2006a; Hurst et al., 2011). However, a benefit of field outcrop analogues is that sub-vertical structures can be mapped at mm-scale resolutions, which is not possible using seismic reflection imaging. Consequently, more accurate quantification of fault/fracture properties, such as measurement of aperture or cement infill type, is achievable using outcrop based studies. The study of outcrops can be complemented with the mapping of a target area, using unmanned aerial vehicles (UAVs) that allow mapping over large distances (km-scale) at very high accuracy (cm-scale). These data can then be used to calculate digital elevation models, image mosaics, and high-resolution point clouds which, once geo-referenced using ground control points, can help close the observational gap between seismic data and geological field sampling.

3.10. Process-based numerical modelling

Process-based numerical modelling, for simplicity called hereafter numerical modelling, can be used to provide quantitative insights into: how chimneys form and propagate through time and space; the distribution and transport of mass (water, CO_2, CH_4, higher hydrocarbons, salts, grains etc.) and energy (heat) components among different phases (solid, liquid, gas) through pores and fractures; the complex coupled physical and chemical processes between the above components and properties; and the changes in petrophysical (e.g., porosity and permeability) and chemical properties (e.g., dissolved gas distribution in the formation fluid brine). Therefore, numerical modelling approaches are useful in helping to quantitatively understand the governing processes that can explain observations, but they are, in turn, reliant on appropriate calibration relating to the target of interest.

As part of the STEMM-CCS and CHIMNEY projects, reactive transport modelling has been conducted (by Marín-Moreno et al., 2019) to examine the migration of injected CO_2 through a generic chimney, using Scanner pockmark as a proxy for pressure, temperature, geological, mineral, and chemical conditions. In the model, the chimney extends upwards in the subsurface reservoir through the cap rock to a shallowest depth of 400 mbsf, where it meets the overburden (Fig. 11a). Modelling was conducted in a radially symmetric geometry approximation, with injection of CO_2 taking place at 500 mbsf and 0 m radial distance. The time scale of this analysis is 100 years, longer than potential geological
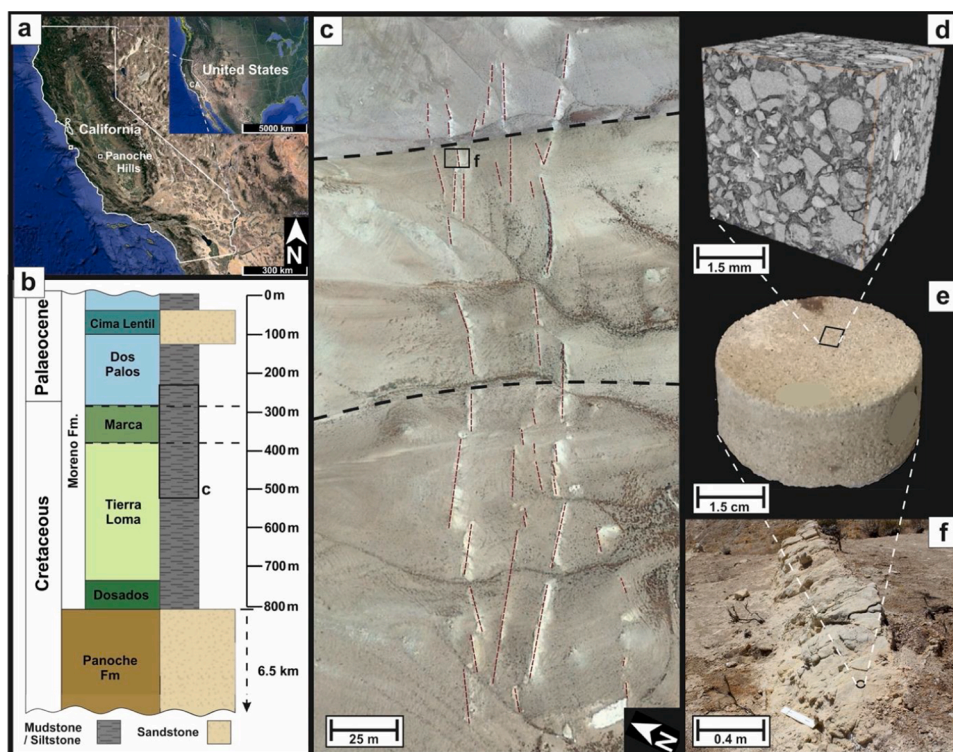
Fig. 8. Field outcrop analogue of a fluid escape system in the Panoche Hills, Central California. a) Map of the Panoche Hills field location. b) Lithostratigraphy of the Panoche Hills which includes the Panoche Fm., comprised of up to 6.5 km of turbiditic sandstone, overlain by greater than 600 m of mudstone and siltstone cap rock/overburden sealing units. c) Map view of sand filled fractures intruding sub-vertically through the sealing units of the Moreno Fm. The map view is analogous to the spatial extent mappable with UAVs. d-f) Direct sampling and observation of a sand-filled fracture at different length scales, which includes d) pore-scale XCT analysis and e) core-scale laboratory analysis.

CO_2 injection activities.

Modelling indicates that, over these timescales, the porosity (Fig. 11b) and permeability (Fig. 11c) changes due to dissolution and precipitation of minerals are negligible for the representative chimney being modelled (Marín-Moreno et al., 2019). Hence, for this particular location and over the time scale of this analysis, the modelling of chemical reactions (Fig. 11d,e) can be dismissed. For injected CO_2 saturations of ≥ 30 %, and with overburden isotropic matrix permeabilities and chimney effective vertical permeabilities (average permeability of the matrix and the fractures in the chimney) of $\geq 10^{-14}$ m^2, the models indicate that CO_2 reaches the seabed, at 500 m above the injection point, in less than 100 years (Fig. 11a,f).

The modelling conducted assumes that the injection of CO_2 occurs far away from the chimney, in isothermal conditions, and that there are no mechanical changes (Marín-Moreno et al., 2019). However, the non-isothermal upwards migration of CO_2 may create stress- and thermal-induced deformations that could affect the aperture of existing fractures, or create new fractures, and so, in turn, affect the migration processes. Thus, assessment of the impact of thermal, hydraulic, and mechanical changes of fractures within chimneys may require further consideration.

The dynamics of fluids migrating within the shallow overburden sediments can also be assessed using a Navier-Stokes-Darcy multi-fluid flow model (AnsdMF), which simulates the mass and momentum exchanges of multi-fluid phases (Behzadi et al., 2004; Bannari et al., 2008) and couples the turbulent flows in the ocean with the flows in sediments (Fig. 12a). The AnsdMF modelling was conducted in 2D, and comprises a sediment layer with a defined thickness, porosity, and fracture properties (length and aperture; Fig. 12b). These subsurface characteristics may be further constrained using other methods discussed in this study. Above the seabed is a turbulent bottom boundary layer. The location and rate of gas release beneath the seabed are then specified and the gas is tracked as it migrates and disperses through the sediment, and is expelled from the seabed (Fig. 12c).

The AnsdMF model is robust and efficient for simulations of multi-fluid flow in sediments with a complex structure and variable fracture properties, and fluid pathways to a turbulent ocean. In addition, AnsdMF can be applied over a wide range of scales, ranging from micro/pore- to field-scale ($\leq 10^{-2}$ to $\geq 10^3$ m). The observations from computational fluid dynamic models can be calibrated against observations derived from active seismics, which provide a measure of fluids expelled from the seabed, and passive seismics, which can additionally detect flow within the subsurface, to compare flux rates of subsurface fluid migration with observed discharge from the seabed. Further, bio-ecosystem models could be coupled with AnsdMF and advanced oceanic hydrodynamic models to assess the impacts of fluid migration on benthic ecosystems and in the water column (Blackford et al., 2020).

4. Discussion - A multi-scale, multi-disciplinary approach

4.1. Parameters

In this paper, a number of methods have been identified which can be utilised and integrated to generate a comprehensive characterisation of subsurface fluid pathways associated with chimneys. The parameters influencing fluid flow within chimneys can be broadly divided into three categories: 1) structural properties including the subsurface stratigraphic structure, the presence, geometry, distribution and connectivity of fractures, and principal stress magnitude and orientation; 2) physical properties of the sediments, including thermal, hydraulic, mechanical, elastic, and electrical properties; and 3) fluids, which includes their presence, phase, and distribution in the subsurface, chemical composition, and volume/mass flux calculations (Table 1; Fig. 13). In general, at least one approach from each of the method groupings (Table 1 left-hand column) is required to reach a sufficiently detailed and holistic understanding of the structure and processes involved in the venting of gas via a chimney.

We have also identified five method traits: resolution, length scale, temporal applicability, co-dependency, and resource use. The method parameters and traits are summarised in Table 1 and are further discussed below.
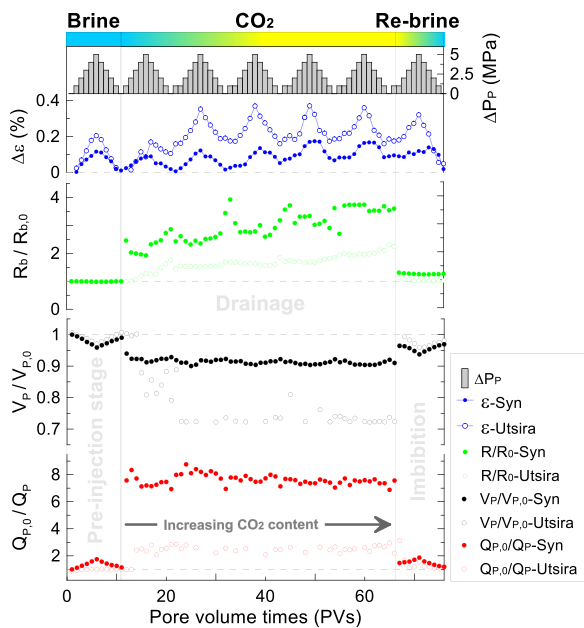
Fig. 9. Laboratory flow-through experimental results. Brine−CO_2 flow-through tests were conducted for two samples, a 38 % porosity synthetic sandstone (Syn) and an intact core sample from Utsira Sand formation (Sleipner field). The tests simulate cyclic overpressure scenarios (ΔP_P) in a Sleipner-like CO_2 storage reservoir during pre-injection, CO_2 injection (drainage) and post-injection (imbibition) stages. Electrical resistivity, P-wave velocity, V_P, and P-wave attenuation, Q_P^{-1}, are normalised with respect to the values at the original reservoir conditions (16.4 and 7 MPa of confining and pore pressure, respectively), and plotted together with volumetric strain, ε_v, versus pore volume (PV, i.e. injected fluid volume normalised to the sample pore volume). The results show the effect of rock consolidation on the elastic and transport properties of reservoir formations with similar petrophysical features but different degrees of cementation (i.e., weakly-cemented Utsira sand formation versus silica-cemented synthetic sandstone), and the evolution with the increasing CO_2 content. Figure adapted from Falcon-Suarez et al. (2018).

4.2. Resolution and scale

Table 2 shows (a) the order of magnitude resolutions and (b) length scales (area and/or depth) achievable for each method applied to the study of a chimney. Table 2a demonstrates that there is a resolution gap between the geophysical (seismic, acoustic, CSEM) and geological/geochemical (rock sampling, laboratory) methods around the m-scale. Numerical modelling approaches allow bridging of the resolution gap, by the integration of data from the geophysical, geological and geochemical methods.

There is an inherent trade-off between resolution and length scale, whereby methods capable of achieving higher spatial resolution can typically only be applied at reduced length scales. This is particularly an issue in the vertical dimension. This trade-off arises in seismic and CSEM studies due to an intrinsic relationship between the imaging resolution and depth scale, whereby lower frequency sources have greater depth penetration, due to the stronger attenuation of higher frequency signals over lower frequencies (Resnick, 1990). However, vertical imaging resolution is also related to bandwidth, with lower bandwidth signals resulting in a lower vertical resolution than higher bandwidth signals. Taking the seismic approaches utilised in this study as an example, the lower frequency airgun sources generate the best depth penetration ($\geq$100 s of m), but are limited to high m to 10 s of m or greater vertical resolution, while sparker sources may only penetrate a few 100 s of m, but can generate m-scale resolution, and sub-bottom profiler recording (which we include here with seismic approaches as they are applied for the same purpose) can achieve resolutions on the dm-scale, but with only very limited (10 s of m) depth penetration. Therefore, where

frequency-dependent attenuation is a factor in measurements made using a particular method, Table 2 must be considered in this context.

An optimal subsurface imaging approach would assess parameters at the highest resolution possible over the areal and depth extent of the chimney. However, where these features are located at depth, beneath overburden and sealing layers, attenuation of higher frequencies results in a depth-resolution trade-off, with increasingly only larger features visible. This represents a key motivation both for the application of a multi-frequency surveying approach in the Scanner pockmark seismic experiment, utilising a range of seismic sources (e.g., airguns, sparkers), and the study location chosen. Together, these allow the development of a cross-scale, sufficiently resolved image of a chimney at shallow depth, where it can be studied in detail, with other techniques (laboratory experiments, numerical modelling) then able to extend the observations to the deeper subsurface, where they may be detected by geophysical techniques at lower resolution. The use of a broad seismic source frequency range for the anisotropy experiment is also critical, due to the frequency dependence of anisotropy detection and interpretation (Chapman, 2003).

In addition, some of the methods display differing sensitivities to the magnitudes of the properties being measured (e.g., Constable, 2010). For example, while the elastic properties of sediments are sensitive to both lithological and pore fluid variations, their electrical resistivity is dominated by the pore fluid component. The differing response of these two techniques as gas saturation varies has been shown by Constable (2010) for a 50 % porosity sand. The largest effect on P-wave velocity occurs for the first few percent of gas fraction and changes very little above this (White, 1977; Lee, 2004). In contrast, the resistivity response increases exponentially with increases in gas saturation (Archie, 1952). As a result, gas saturations determined using seismic and CSEM methods may differ (e.g., Goswami et al., 2015; Attias et al., 2020; Bialas et al., 2020), with CSEM being more sensitive to the wider saturation-range response measurable.

4.3. Temporal applicability

The integrated methods described in this paper also influence the temporal scales over which fluid flow through chimneys can be understood (Table 1). Only a few of the methods can be used to determine temporal information related to pore fluid changes in the subsurface (measured at discrete time intervals using time-lapse/4D seismic), fluxes through the subsurface (measured discretely by active acoustics, and measured/modelled continuously using passive seismics and computational fluid dynamics), and fluid-induced chemical and physical changes (geochemical methods and numerical modelling).

Repeat geochemical data collection and seismic surveying can be conducted, commonly on the time scale of every year or few years. However, measurement of true temporal changes using seismic data, rather than seismic artefacts, is limited by the repeatability of the surveying technique. This makes time-lapse seismic studies most suitable for application to areas of well stratified and undisturbed sediments, rather than chaotic features such as chimneys (e.g., Waage et al., 2019). Developments in time-lapse seismic repeatability, such as continued use of true-4D imaging, or the installation of permanent seabed sensing infrastructure such as OBS or fibre optic cables, have the potential to improve this.

Passive seismic and active acoustics can resolve temporal flow variations on the order of seconds to weeks, providing information on the ascent of individual bubbles, but also how flow is modulated by diurnal tides. Of these, however, only passive seismic provides continuous temporal information over extended periods of time. These two methods have, therefore, different applicabilities to short- and longer-term monitoring activities of fluid escape associated with chimneys. Both methods also play an important role in the calibration of computational fluid dynamic models of fluid migration through the chimney and out of the seabed. These models can then be adapted to provide further
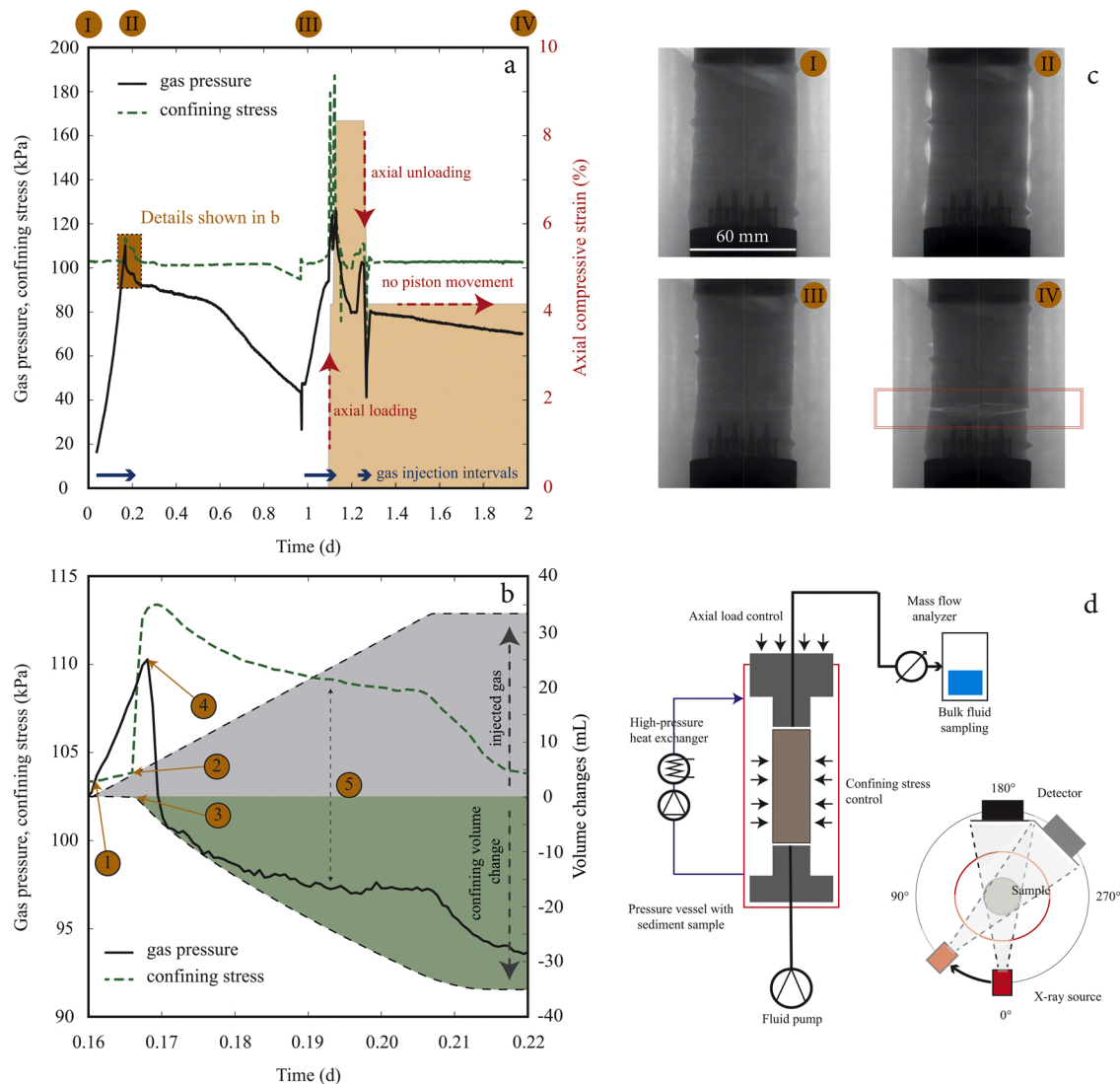
Fig. 10. Fracture formation due to gas migration in poorly consolidated clay sediments. Flow through experiments were carried out on gravity core samples recovered during RV Poseidon cruise POS534 (Schmidt, 2019). Injection experiments were carried out with N_2 because of its low solubility compared to CO_2. a) Gas pressure and confining stress. b) Pressure-volume relations during and after fracture formation. c) X-ray projection images at different time points. d) Setup of the X-ray micro-CT imaging system. Gas was injected in intervals (dark blue arrows) followed by pressure dissipation periods. Fracture formation was rapid after gas pressure increased above the confining stress (1). After reaching a critical pressure for fracture formation, an increase in confining stress (2) triggered confining fluid removal (3). The gas pressure dissipated rapidly after fracture opening (4), which subsequently resulted in the accumulation of gas at the sample surface. The offset between confining stress and gas pressure during ongoing gas injection (5) likely resulted from measurement inaccuracies because all system components were rated for high-pressure operation.

information about the temporal evolution of fluid flow processes through chimneys in different geological settings.

Of the methods that can be used to assess changes in the properties of chimneys over time, only numerical modelling approaches can be extended to much longer timescales (centuries to millennia), compared to experimental, field or laboratory techniques. Field-based outcrop analysis may also be considered to provide additional temporal information, allowing understanding of flow over geological timescales, long after active flow has ceased. However, the integration of these techniques enables the development of new multiscale coupled seismic-hydro-mechano-chemical modelling approaches, with the potential of enhancing predictions of chimney behaviour over time.

4.4. Co-dependencies

Table 1 shows that a range of geophysical methods can be used to determine the site parameters of interest to the study of fluid flow structures. However, the successful application of individual methods relies on a network of co-dependencies between different methods for calibration and constraint (Table 1). In particular, inverse methods, such as travel time tomography and CSEM, are subject to inherent trade-offs between model parameters, such as velocity or resistivity respectively, and layer thickness (Edwards, 1997). Travel time tomography is also problematic when trying to resolve low velocity zones, as the energy is diverted away from them. As a result, use of prior geological knowledge, or constraints from other data, is important in the modelling process (e. g., Harris et al., 2009; Goswami et al., 2015; Attias et al., 2016).

Some co-dependencies are more significant than others. Seismic reflection imaging provides constraints on several of the methods utilised in this study, which explains its widespread use in subsurface exploration and monitoring programmes. Seismic reflection imaging and seismic inversion are co-dependent, although it is possible for these methods to be deployed fully independently. It is advantageous for travel time tomography to have input from reflection imaging of the
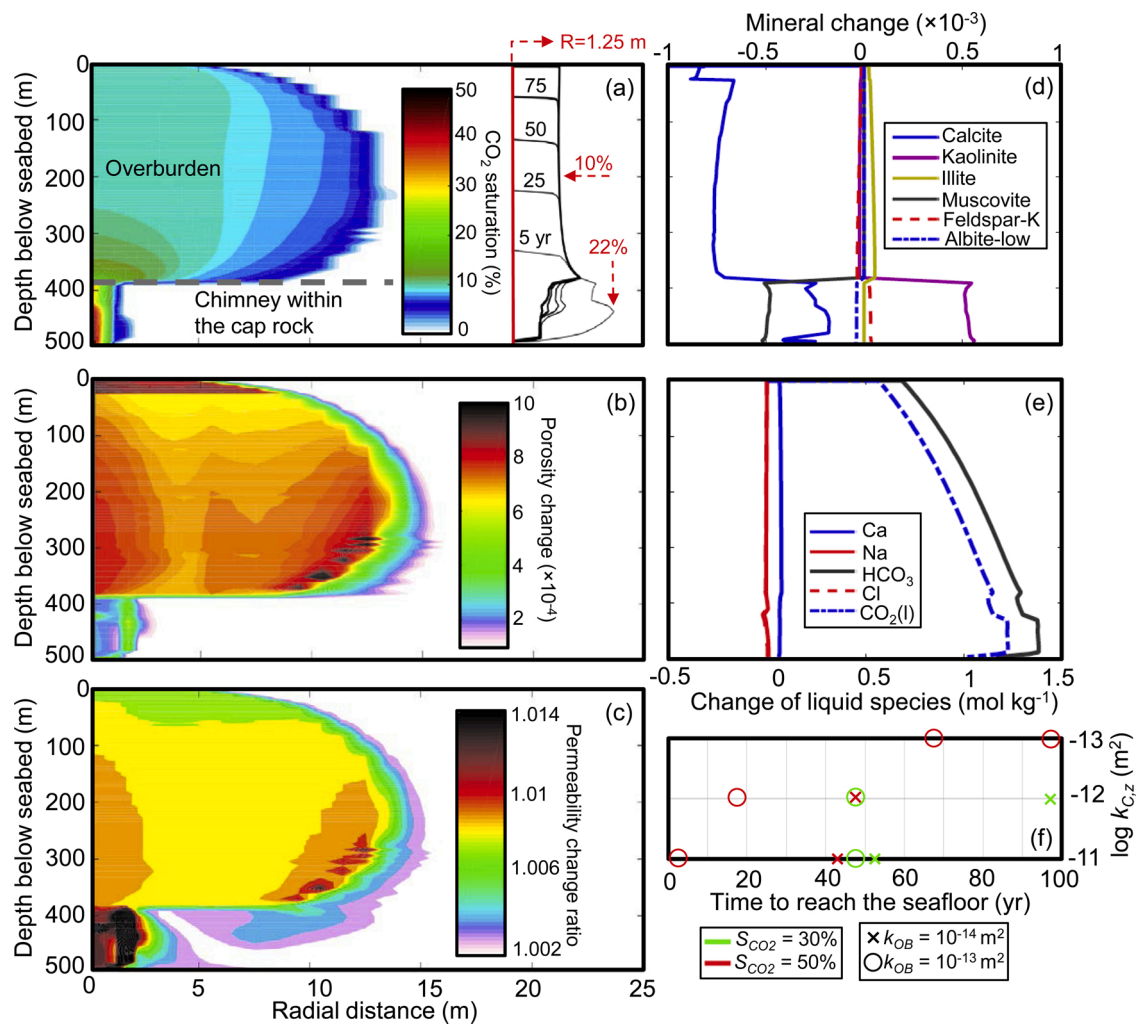
Fig. 11. Reactive transport modelling of CO_2 migration through a generic chimney using the North Sea, Scanner pockmark complex as a proxy for pressure, temperature, geological, mineral, and chemical conditions. The model geometry comprises CO_2 injection at a radial distance of 0 m and depth below seabed of 500 m. The chimney extends vertically to the top of the cap rock (400 mbsf). Results are shown after 100 yr, with a constant injected CO_2 saturation of 50 %, an overburden isotropic permeability of 10^{-13} m^2 and chimney vertical and horizontal permeabilities of 10^{-13} m^2, and 10^{-15} m^2. Variation of a) CO_2 saturation, b) porosity and c) permeability with depth and radial distance. Inset in a) shows the temporal evolution over 100 yr of CO_2 saturation with depth at a distance of 1.25 m from the injection point. Red numbers are CO_2 saturations. Changes in d) mineralogy and e) concentration of liquid species at a distance of 1.25 m from the injection point. f) Models of CO_2 gas reaching the seabed in less than 100 yrs for tested injected CO_2 saturations of 10 %, 30 %, and 50 %; overburden isotropic permeabilities of 10^{-13} m^2, and 10^{-14} m^2; and chimney vertical permeabilities ranging from 10^{-11} m^2 to 10^{-16} m^2 (ratios of chimney vertical to horizontal permeability from 1 to 1000 were tested). Figure adapted from Marín-Moreno et al., 2019.
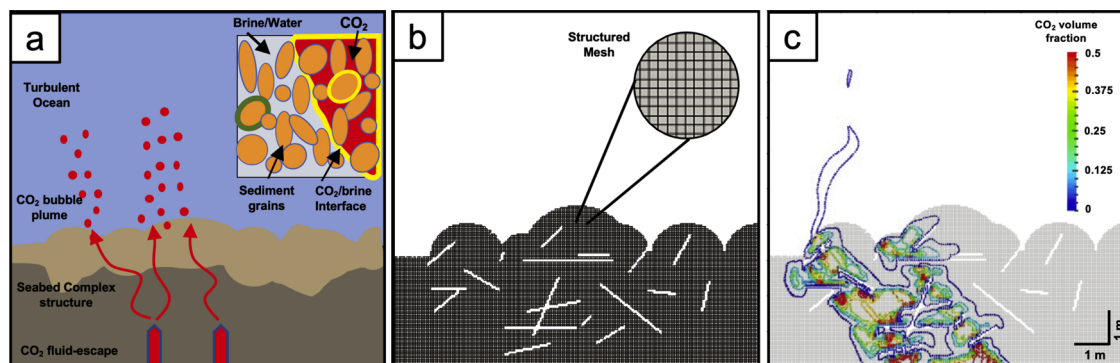
Fig. 12. Computational fluid dynamic modelling of gas leakage through sub-seabed fracture network. Modelling has been conducted for CO_2 fluid escape. (a) Schematic of complex subsurface sediments, gas plume at a potential fluid escape site. (b) Simulation geometry. Lower (black) part of model is sediment (~4 m average thickness) with 1 cm thick, non-connected fractures (white). Upper part is the water column. c) Contoured gas volume fraction at time (snapshot) of gas dispersion through sediments into the ocean. Figure adapted from Saleem (2020).
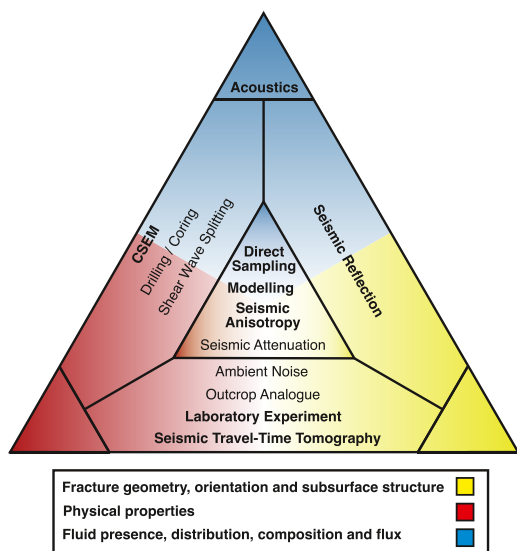
Fig. 13. Summary of relationships between methods used and parameters investigated in the study of the chimney beneath Scanner pockmark. Triangle plot highlighting the three main parameters (Table 1) used for characterisation of a chimney/fluid escape system, where each method is located within the regions of the triangle corresponding to the parameters it can be used to resolve.

subsurface in order to constrain the solution of the non-unique tomographic problem towards realistic subsurface structures. However, it is also important that modelling is conducted in an objective manner that does not overly bias the result, and suitable modelling approaches can be applied which do not require/depend on this additional starting constraint. The velocity information which is obtained from travel time tomography or FWI can be used to improve the quality of seismic reflection imaging, including assisting with migration and depth conversion, in which accurate interval velocity information plays a central role. Furthermore, it can provide velocity information in areas of seismic blanking or potential artefacts, such as those associated with the presence of gas in the chimney. Converted-wave seismic anisotropy may also be partially reliant on seismic reflection data, to identify seismic horizons where mode conversion may occur, and an independent shear-wave velocity constraint is also required to interpret from which layers these signals may be originating, and for layer-stripping (Haacke and Westbrook, 2006).

Laboratory experimental approaches can provide insights into the dominant processes governing the response of the system. The experimental strategy and the ability to approximate the real behaviour of subsurface chimneys, or other subsurface fluid migration pathways, depends on suitable calibration and constraints from field geophysical and geochemical experiments. Laboratory experiments are directly dependent on the quality of direct sampling. One way to minimise this dependency is to use synthetic samples to replicate subsurface material. In the study of Scanner pockmark, the main limitation of direct sampling was dewatering of the water saturated, poorly consolidated samples that

Table 2
Summary of the resolution (a) and the length scale (b) over which each geophysical method can be used to assess parameters, for complete characterisation of chimneys. Note that for methods subject to frequency-dependent attenuation with increasing depth penetration (e.g., seismic, CSEM), we show here the full range of resolutions and length scales. Thus, as depth penetration increases, the smallest achievable resolution and length scale will also increase.

a)

Methods		Resolution					
		≤cm	dm	m	10s m	100s m	km
Acoustic (A)	Active acoustic			█	█		
Passive seismic (PS)	Passive seismic				n/a		
Seismic reflection (SR)	2D / 3D / time-lapse reflection		█	█	█	█	
Seismic tomography (ST)	Travel time tomography & FWI			█	█	█	█
Seismic anisotropy (SA)	Shear wave splitting				█	█	
	Seismic attenuation				█		
	Ambient noise anisotropy					█	█
Controlled source electromagnetics (CSEM)	CSEM				█	█	█
Direct sampling (DS)	Drilling & core analysis	█	█				
	Outcrop analogues	█	█				
Laboratory experiments (LE)	Laboratory experiments	█					
Modelling (M)	Numerical modelling	█	█	█	█	█	█

b)

Methods		Length Scale					
		≤cm	dm	m	10s m	100s m	km
Acoustic (A)	Active acoustic			█	█	█	
Passive seismic (PS)	Passive seismic			█	█	█	
Seismic reflection (SR)	2D / 3D / time-lapse reflection			█	█	█	█
Seismic tomography (ST)	Travel time tomography & FWI				█	█	█
Seismic anisotropy (SA)	Shear wave splitting				█	█	█
	Seismic attenuation				█	█	█
	Ambient noise anisotropy				█	█	
Controlled source electromagnetics (CSEM)	CSEM			█	█	█	█
Direct sampling (DS)	Drilling & core analysis	█	█	█	█		
	Outcrop analogues	█	█	█	█	█	
Laboratory experiments (LE)	Laboratory experiments	█	█	█			
Modelling (M)	Numerical modelling	█	█	█	█	█	█

likely occurred during the core extraction process, leading to alterations in the physical properties of the core material. Future optimisation of the core extraction process is required, to ensure improved preservation of poorly consolidated cored material. Autoclave pressure coring tools could be used, such as the IODP Pressure Core Sampler (Graber et al., 2002) or MeBo-MDP (Pape et al., 2017), that are able to retrieve sections of a drill core under in-situ pressure, thereby avoiding disturbances of the cored sediment due to degassing that occur during conventional coring. Hence, pressure coring permits the investigation of cored materials whilst retaining the in-situ physical, structural, and chemical properties (e.g., permeability, gas content, resistivity, salinity). Furthermore, the acquisition of borehole geophysical measurements (e. g., cross borehole surveys using wireline logging tools) is another common method for obtaining in-situ measurements, provided that the drilled borehole is stabilised by a liner (e.g., Crain, 2010). The results from rock physics experiments can be used to derive and validate the results of travel time tomography, FWI, and seismic anisotropy studies.

Multiphase and multicomponent numerical modelling of the thermal, hydrological, mechanical, and chemical response of marine geological systems with chimneys is currently limited by the robustness of available in-situ geophysical and chemical characterisation methods, especially for fracture geometrical, physical, and chemical properties, and the difficulty in accurately recreating these in the models. How well individual processes are represented in the numerical modelling results depends strongly on the in-situ geophysical and geochemical data available to constrain the model input parameters. This further highlights that an appropriate direct rock sampling strategy is an essential part of the multi-disciplinary approach for chimney characterisation.

Active acoustic and passive seismic methods for detecting fluid flow can be applied independently of other approaches (Fig. 13). A water-column sound velocity profile is required for accurate calibration of the shipboard echo-sounders, and, depending on the subsurface geological structure, a detailed velocity model may be necessary for accurate relocation of micro-seismic events. Cross-calibration of these two approaches is important, in order to extend the temporal observations of more punctual active acoustic surveys, and to resolve ambiguities in the apparent response of different bubble size distributions. These approaches also provide an important calibration for computational fluid dynamic modelling, either by indicating the potential flux entering the modelled system or measuring the expulsion from the seabed.

4.5. Resource use, challenges and development

It is also important to consider resource demand in the study of focused fluid flow conduits, such as the chimneys at Scanner pockmark, and how this may impact future studies relevant to CCS operations. Resources may include both direct monetary costs associated with data acquisition, in addition to less-well defined time-based costs, which cover the data processing and interpretation. Ultimately, there is a trade-off between the field experimental methods which can be performed using a given set of resources (including time), and the total amount of information which can be determined about the subsurface structure.

Offshore site characterisations are generally spatially discrete snapshots in time. Undertaking studies of this nature requires field expeditions, including ship time, which results in relatively high monetary costs. Furthermore, the spatially discrete nature of offshore site investigations means that subsurface information must be gathered from all potential future sites of interest to CCS, to understand the geometry of the structures that may be present.

Depending on the availability of prior information about the specific imaging target, such as its spatial and depth scale, and the practicalities of implementing different imaging techniques, it may be possible to conduct experiments where multiple data sets are acquired concurrently, reducing the time-cost of the operation. For example, during the cruise JC152 seismic experiments at Scanner pockmark both the travel time tomography and seismic anisotropy datasets were collected using the same sets of shots, while the GI, Duraspark and Squid sparker sources were also recorded using a towed seismic streamer. Passive seismicity, for the study of fluid migration through the subsurface and ambient noise, was recorded using the same OBS array as for the JC152 tomography and anisotropy experiments (Fig. 3a). However, the parameters of a single seismic experiment may not be able to ideally meet the needs of all the different types of analysis that may be required for full and detailed characterisation of the subsurface feature(s) of interest. For example, for ambient noise studies, larger OBS station spacings would allow lower frequencies to be utilised in the analysis (e.g., Rost and Thomas, 2009). However, this conflicts with the smaller spacing required to achieve the maximum shallow subsurface resolution in tomographic models.

In a number of cases, the time-based cost of the techniques described in this study is relatively low, due to the relative simplicity of data processing using well-established methods (e.g., seismic reflection data, active seismics, core/field sample analysis). However, while many of the methods discussed in this study are well-established and extensively used in both research and industrial settings, there is potential for future reductions in resource costs. Methods such as travel time tomography, CSEM, passive seismics, and seismic anisotropy involve significant time in manual data picking and/or modelling, resulting in high relative time costs. Future developments in data processing may permit the replacement of manual processing stages with automated workflows, which may be facilitated by machine learning and artificial intelligence (e.g., Kim and Nakata, 2018; Kong et al., 2019), resulting in reduced time costs. Further, from the geophysical experiments at Scanner pockmark, it can be determined that significant processing time could be saved if OBS and OBEM spatial coordinates, degree of tilt, and orientations are more accurately constrained during data acquisition (e.g., Haacke and Westbrook, 2006). Installing permanent OBSs or fibre optic cables would allow easier and more cost-effective implementation of repeat seismic surveying, where multiple cruise legs are required. Compared to offshore exploration costs, laboratory experiments can be run at much lower expense, especially the measurement of basic parameters, while the investigation of the effect of parameter changes (e.g., temperature, pressure) on the system may also be tackled using carefully designed experiments.

Ultimately, the STEMM-CCS and CHIMNEY studies of the chimneys at Scanner pockmark provided significant information on the structure of these features, which may be applied in future studies. The multi-scale and multi-parameter design of these investigations demonstrates that the integration of subsurface geophysical characterisation of a chimney with laboratory experiments, process-based numerical modelling approaches, and onshore analogues is possible. We also anticipate that our findings will be applicable for future targets, in particular those located at depth, beneath the overburden and sealing cap rocks, where higher resolution subsurface imaging is much more challenging. Therefore, the findings of the STEMM-CCS and CHIMNEY projects have the potential to reduce future resource intensiveness, whereby the pre-existing knowledge of fluid flow systems gained from studying the Scanner pockmark complex can be applied to new sites, reducing the need for additional site specific data acquisition.

5. Relevance to geological CO_2 storage

The study of chimneys as potential fluid flow systems is highly relevant to the risk assessment of future CCS operations. For the assessment of a prospective CO_2 storage site, a site characterisation is first conducted to understand the potential containment risks, based on pre-existing seismic, well, and environmental baseline data (e.g., Furre et al., 2019b). As the project progresses in maturity, additional data may be acquired based on identified risks or uncertainties. Containment risks are commonly identified using a bowtie risk assessment, where monitoring and modelling activities are implemented as barriers to reduce

the likelihood of a top event (Dean and Tucker, 2017). A top event may be described as the unintended migration of CO_2 from a primary or a secondary sealing layer. In this context, chimneys could be considered as one such risk element. Fluid escape through abandoned/legacy wells and faults are other common risk elements that require consideration (IPCC, 2005).

If chimneys are identified as a potential threat from the initial site characterisation (based on existing data), stakeholders would be required to follow a process to determine unknown parameters which may contribute to the containment risk. Fig. 14 demonstrates a potential approach to this, where the findings of our multi-scale approach to determining chimney parameters (Section 4; Tables 1 and 2) are integrated into an existing Measurement, Monitoring and Verification (MMV) risk-based decision framework (Dean and Tucker, 2017). The outstanding risk question is defined as specifically as possible, and the unknown factors which contribute to this are separated from the parameters which are sufficiently well resolved from pre-existing resources. The remaining unknown factors, which may include fracture connectivity, permeability, and/or fluid volume flux and composition, are then targeted using appropriate methods drawn from Section 3, in order to mitigate the outstanding risks. The selection of which method(s) to use is based on each methods' suitability for determining the parameters of interest (Table 1; Fig. 13), at the appropriate resolution and scale for the problem (Table 2), and any potential dependencies it may have (Table 1). Tailored deployment of new resources is then conducted, in a monitoring step. This may, for example, involve further data acquisition and/or modelling studies. Alternatively, this could also include the re-processing or re-appraisal of existing data or models. In order to optimise the risk assessment process, this step should factor both the additional cost and time of further acquisition against the benefits of obtaining the new information using these approaches. The staging of resource deployment is also important at this stage, such that the maximum amount of new information is resolved using the minimum necessary additional resource cost/time. It would not, therefore, necessarily be either feasible or desirable to use all of the methods discussed in this study, highlighting that stakeholders need to efficiently determine the parameter-specific traits they require for appropriate de-risking of the chimney. The outcomes of the monitoring step are then used to re-appraise and verify the containment risk-level attributed to the chimney, before a decision is made. If this verification stage indicates that all of the outstanding risks have not yet been constrained

sufficiently, the process should be repeated until they have. In this respect, the risk assessment and mitigation process can be considered to be a cycle (Fig. 14).

Each prospective CO_2 storage site will have unique characteristics and, therefore, will be different. However, potential risks need to be assessed holistically, which will result in different resource deployment choices for different sites. Based on the outline workflow we have described, and using Tables 1 and 2 as a guide, we can consider a number of simple examples which could be resolved using this approach. If a fracture network at a spatial scale of 10 s of m was deemed to be the greatest threat/uncertainty for prospective CCS operations, then seismic reflection or seismic tomography would be the most suitable method to use, while CSEM data may also assist in determining fracture connectivity and fluid content. If the sediment matrix porosity-permeability or the effects of microfractures were the principal cause of concern, laboratory experiments and/or modelling, using appropriate field analogues to define the input parameters, would be the optimal approach. As a final example, if CO_2 emission and flux rate from the seabed over a spatial scale of >1 km were the greatest threat/uncertainty, active acoustics would be the most appropriate method to use.

Alternatively, further data acquisition may not be required. In the case of the Goldeneye prospective storage site, located in the Outer Moray Firth Basin, Central North Sea, a chimney-like feature was observed during the risk assessment phase. However, rather than further data acquisition, the first monitoring step applied was to conduct high resolution re-processing of existing data, alongside pre-stack interpretation. Together, these approaches resolved the issue sufficiently, finding that the observed feature instead represented a seismic imaging artefact caused by a glacial tunnel valley, without the need to acquire additional data (Dean et al., 2015).

Active natural methane escape is observed directly within the shallow subsurface of the exemplar chimney at the Scanner pockmark complex in the North Sea. However, prospective CO_2 storage reservoirs are more commonly located at greater depth and are capped by several sealing layers, for example the storage units at Sleipner are located at a depth of $\sim800-1000$ mbsf. Therefore, understanding the role of chimneys in applied CCS environments may also represent a deeper subsurface problem. Compared to shallow chimneys, deeper chimneys may exhibit a number of differences, such as 1) increased stress - fluid pressure - temperature conditions; 2) the fluid of interest may be in a different phase (liquid compared to gas); and 3) changes in the sediment
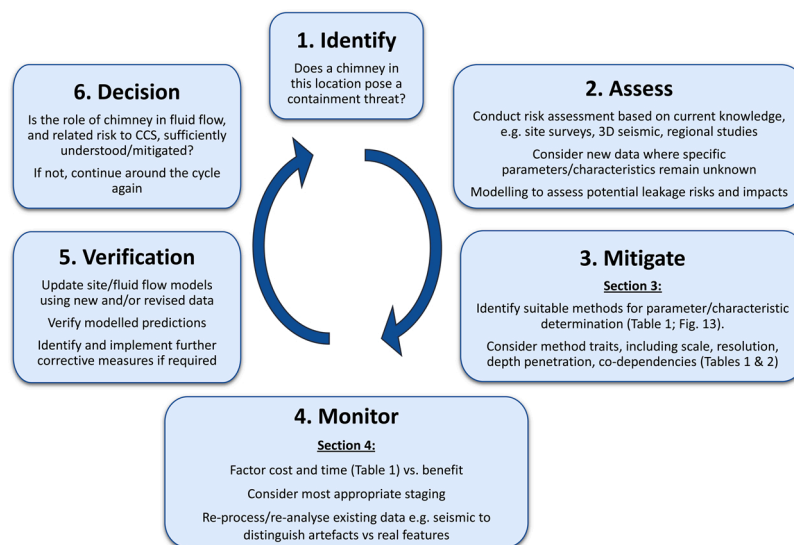

Fig. 14. Outline of a decision-making cycle illustrating the steps in the risk-based assessment of a site where chimneys may pose a risk to potential CCS operations. The multi-parameter, multi-scale approach discussed in Sections 3 and 4 of this paper should be used in steps 3 and 4, the mitigating and monitoring steps, in order to optimise the decision making process.

and pore fluid composition. At greater depths (higher effective stresses) there is likely to be more consolidated material, which may result in reduced porosity-permeability of the sediment matrix. Moreover, fracture apertures tend to decrease with increasing effective stress (increasing depth). Therefore, if a chimney existed at greater depths, it is more likely to have lower effective permeability, although this is dependent on the rock material properties and microscopic fracture roughness (e.g., McDermott and Kolditz, 2006; Rutqvist, 2015). At greater depths the chimney would need to contain considerable stress-persistent fracture apertures to be deemed a risk. Further research is required to more accurately constrain the differences expected between deeper and shallower chimneys. The study of deeper chimneys may also alter the experimental approach. For example, a number of the applied geophysical methods lose resolution with depth, due to the increasing attenuation of higher frequency signals that are required to image structures at shorter length scales (Resnick, 1990). However, by applying the principles discussed here and in Fig. 14, a multi-component, appropriate target-scale risk appraisal approach can be developed for a chimney structure located at greater depth.

Overall, our integrated multi-scale experimental approach can be incorporated into pre-existing measurement, monitoring and verification approaches (e.g., Dean and Tucker, 2017). Future monitoring approaches must also be supported by robust baseline surveys and detailed understanding of the risks of CO_2 emissions that extend into the marine environment (Blackford et al., 2014, 2015; Flohr et al., 2021). Our understanding of fluid flow through chimneys must be improved to decrease containment risks at prospective storage sites and thereby realise the potential of CCS for mitigating global warming.

6. Summary

Chimneys (also referred to as seismic chimneys and/or pipes) may represent an important class of subsurface fluid escape pathway. The study and understanding of chimneys are highly important to risk assessments for potential CCS applications. To this end, the STEMM-CCS and CHIMNEY research programmes have investigated chimneys in the North Sea. The results of these investigations will contribute to the further development of models for the understanding of fluid flow through such structures.

In this paper we have described an approach for the multi-scale, multi-method geophysical characterisation of chimneys within sedimentary basins, using the Scanner pockmark as a case study. In the development of this multi-method approach, we note the following:

- While individual experimental approaches, conducted in the field or in the lab, are able to determine one or more of the physical properties of chimneys and their role in fluid flow, integration between different methods is required to fully characterise the system.
- Many of the described approaches rely on having suitable constraints and calibration from other methods. It is necessary, therefore, to ground-truth the methods, both in the field and in the laboratory, wherever possible, in order to ensure that conclusions determined are robust.
- The method approaches available are applicable at different physical length scales and resolution, with a common trade-off between these two factors. Hence, it is also important that the techniques used to study fluid flow structures are applied across scale and resolution ranges, as well as different temporal scales, in order to build a holistic and sufficiently detailed understanding.
- We propose that the integrated methodology presented to study the chimney beneath Scanner pockmark is applicable beyond this specific study area, and thus our work contributes to a wider understanding of this class of feature and its potential importance in fluid migration.

Declaration of Competing Interest

The authors declare that they have no known competing financial interests or personal relationships that could have appeared to influence the work reported in this paper.

References

Achterberg, E., Esposito, M., 2018. RV POSEIDON Fahrtbericht / Cruise Report POS527: Baseline Study for the Environmental Monitoring of Subseafloor CO2 Storage Operations, Kiel-Kiel (Germany), 15.8.-3.9.2018. https://doi.org/10.3289/geomar_rep_ns_45_2018.

ACT Acorn Consortium, 2018. D08 East Mey CO2 Storage Site Development Plan 10196ACTC-Rep-26-01. https://actacorn.eu/sites/default/files/ACT%20Acorn%20East%20Mey%20CO2%20Storage%20Site%20Storage%20Development%20Plan%201.0.pdf.

Alvizuri, C., Tanimoto, T., 2011. Azimuthal anisotropy from array analysis of Rayleigh waves in Southern California. Geophys. J. Int. 186 (3), 1135–1151. https://doi.org/10.1111/j.1365-246X.2011.05093.x.

Amalokwu, K., 2016. Saturation Effects on Frequency-dependent Seismic Anisotropy in Fractured Porous Rocks. Doctoral thesis. University of Southampton, p. 168. http://eprints.soton.ac.uk/id/eprint/391107.

Amalokwu, K., Papageorgiou, G., Chapman, M., Best, A.I., 2017. Modelling ultrasonic laboratory measurements of the saturation dependence of elastic modulus: new insights and implications for wave propagation mechanisms. Int. J. Greenh. Gas Control. 59, 148–159. https://doi.org/10.1016/j.ijggc.2017.02.009.

Andresen, K.J., 2012. Fluid flow features in hydrocarbon plumbing systems: What do they tell us about the basin evolution? Mar. Geol. 332, 89–108. https://doi.org/10.1016/j.margeo.2012.07.006.

Andrews, I.J., Long, D., Richards, P.C., Thomson, A.R., Brown, S., Chesher, J.A., McCormac, M., 1990. The Geology of the Moray Firth, Vol. 3. HMSO, London. http://pubs.bgs.ac.uk/publications.html?pubID=B01844.

Archie, G.E., 1952. Classification of carbonate reservoir rocks and petrophysical considerations. Am. Assoc. of Pet. Geol. Bull. 36 (2), 278–298. https://doi.org/10.1306/3D9343F7-16B1-11D7-8645000102C1865D.

Arntsen, B., Wensaas, L., Løseth, H., Hermanrud, C., 2007. Seismic modeling of gas chimneys. Geophysics 72 (5), SM251–SM259. https://doi.org/10.1190/1.2749570.

Arts, R., Eiken, O., Chadwick, A., Zweigel, P., Van der Meer, L., Zinszner, B., 2004. Monitoring of CO2 injected at sleipner using time lapse seismic data. Greenhouse Gas Control Technologies-6th International Conference 347–352. https://doi.org/10.1016/j.energy.2004.03.072.

Attias, E., Weitemeyer, K., Minshull, T.A., Best, A.I., Sinha, M., Jegen-Kulcsar, M., Hölz, S., Berndt, C., 2016. Controlled-source electromagnetic and seismic delineation of subseafloor fluid flow structures in a gas hydrate province, offshore Norway. Geophys. J. Int. 206 (2), 1093–1110. https://doi.org/10.1093/gji/ggw188.

Attias, E., Amalokwu, K., Watts, M., Falcon-Suarez, I.H., North, L., Hu, G.W., Best, A.I., Weitemeyer, K.M., Minshull, T.A., 2020. Gas hydrate quantification at a pockmark offshore Norway from joint effective medium modelling of resistivity and seismic velocity. Mar. Pet. Geol. 113, 104151 https://doi.org/10.1016/j.marpetgeo.2019.104151.

Baasch, B., Müller, H., von Dobeneck, T., Oberle, F.K., 2017. Determination of grain-size characteristics from electromagnetic seabed mapping data: a NW Iberian shelf study. Cont. Shelf Res. 140, 75–83. https://doi.org/10.1016/j.csr.2017.04.005.

Bachu, S., 2000. Sequestration of CO_2 in geological media: criteria and approach for site selection in response to climate change. Energy Convers. Manage. 41 (9), 953–970. https://doi.org/10.1016/S0196-8904(99)00149-1.

Bahorich, M., Farmer, S., 1995. 3-D seismic discontinuity for faults and stratigraphic features: the coherence cube. Lead. Edge 14 (10), 1053–1058. https://doi.org/10.1190/1.1437077.

Baird, A.F., Kendall, J.M., Angus, D.A., 2013. Frequency-dependent seismic anisotropy due to fractures: fluid flow versus scattering. Geophysics 78, WA111–WA122. https://doi.org/10.1190/geo2012-0288.1.

Bannari, R., et al., 2008. Three-dimensional mathematical modeling of dispersed two-phase flow using class method of population balance in bubble columns. Comput. Chem. Eng. 32 (12), 3224–3237. https://doi.org/10.1016/j.compchemeng.2008.05.016.

Barkved, O., Buer, K., Halleland, K.B., Kjelstadli, R., Kleppan, T., Kristiansen, T., 2003. 4D seismic response of primary production and waste injection at the valhall field. In: 65th EAGE Conference & Exhibition (pp. cp-6). European Association of Geoscientists & Engineers. https://doi.org/10.3997/2214-4609-pdb.6.A22.

Batsi, E., Tsang-Hin-Sun, E., Klingelhoefer, F., Bayrakci, G., Chang, E.T.Y., Lin, J.-Y., et al., 2019. Nonseismic signals in the ocean: indicators of deep sea and seafloor processes on ocean-bottom seismometer data. Geochem. Geophys. Geosystems 20, 3882–3900. https://doi.org/10.1029/2019GC008349.

Batzle, M.L., Han, D.H., Hofmann, R., 2006. Fluid mobility and frequency-dependent seismic velocity — Direct measurements. Geophysics 71 (1). https://doi.org/10.1190/1.2159053.

Bayrakci, G., Scalabrin, C., Dupré, S., et al., 2014. Acoustic monitoring of gas emissions from the seafloor. Part II: a case study from the Sea of Marmara. Mar. Geophys. Res. 35, 211–229. https://doi.org/10.1007/s11001-014-9227-7.

Behzadi, A., Issa, R.I., Rusche, H., 2004. Modelling of dispersed bubble and droplet flow at high phase fractions. Chem. Eng. Sci. 59 (4), 759–770. https://doi.org/10.1016/j.ces.2003.11.018.

Bensen, G.D., Ritzwoller, M.H., Barmin, M.P., Levshin, A.L., Lin, F., Moschetti, M.P., Shapiro, N.M., Yang, Y., 2007. Processing seismic ambient noise data to obtain reliable broad-band surface wave dispersion measurements. Geophys. J. Int. 169 (3), 1239–1260. https://doi.org/10.1111/j.1365-246X.2007.03374.x.

Benson, S.M., Cole, D.R., 2008. CO2 sequestration in deep sedimentary formations. Elements 4, 325–331. https://doi.org/10.2113/gselements.4.5.325.

Berndt, C., 2005. Focused fluid flow in passive continental margins. Philos. Trans. Math. Phys. Eng. Sci. 363 (1837), 2855–2871. https://doi.org/10.1098/rsta.2005.1666.

Berndt, C., Elger, J., Böttner, C., Gehrmann, R., Karstens, J., Muff, S., et al., 2017. RV Maria S. Merian fahrtbericht/cruise report MSM63-Permo. Southampton–Southampton (UK). https://doi.org/10.3289/GEOMAR_REP_NS_37_2017, 29.04.-25.05.2017.

Berndt, C., Chi, W.C., Jegen, M., Lebas, E., Crutchley, G., Muff, S., et al., 2019. Tectonic controls on gas hydrate system of SW Taiwan. J. Geophys. Res. Solid Earth 146 (1). https://doi.org/10.1029/2018JB016213, 54–21.

Bialas, J., Bohlen, T., Dannowski, A., Eisenberg-Klein, G., Gassner, L., Gehrmann, R., Heeschen, K., Hölz, S., Jegen, M., Klaucke, I., Krieger, M., Mann, J., Müller, Ch, Prüßmann, J., Schicks, J., Schünemann, E., Schwalenberg, K., Sommer, M., Smilde, P.L., Spangenberg, E., Trappe, H., Zander, T., 2020. Joint interpretation of geophysical field experiments in the danube deep-sea fan, Black Sea. Mar. Pet. Geol. 121 https://doi.org/10.1016/j.marpetgeo.2020.104551.

Blackford, J., Stahl, H., Bull, J.M., Bergès, B.J.P., Cevatoglu, M., Lichtschlag, A., Connelly, D., James, R.H., Kita, J., Long, D., Naylor, M., Shitashima, K., Smith, D., Taylor, P., Wright, I., Akhurst, M., Chen, B., Gernon, T.M., Hauton, C., Hayashi, M., Kaieda, H., Leighton, T.G., Sato, T., Sayer, M.D.J., Suzumura, M., Tait, K., Vardy, M. E., White, P.R., Widdicombe, S., 2014. Detection and impacts of leakage from sub-seafloor deep geological carbon dioxide storage. Nat. Clim. Chang. 4, 1011–1016. https://doi.org/10.1038/nclimate2381.

Blackford, J., Bull, J.M., Cevatoglu, M., Connelly, D., Hauton, C., James, R.H., Lichtschlag, A., Stahl, H., Widdicombe, S., Wright, I.C., 2015. Marine baseline and monitoring strategies for carbon dioxide capture and storage (CCS). Int. J. Greenh. Gas Control 38, 221–229. https://doi.org/10.1016/j.ijggc.2014.10.004.

Blackford, J., Alendal, G., Avlesen, H., Brereton, A., Cazenave, P.W., Chen, B., Dewar, M., Holt, J., Phelps, J., 2020. Impact and detectability of hypothetical CCS offshore seep scenarios as an aid to storage assurance and risk assessment. Int. J. Greenh. Gas Control 95 https://doi.org/10.1016/j.ijggc.2019.102949.

Blomqvist, S., 1985. Reliability of core sampling of soft bottom sediment—an in-situ study. Sedimentology 32 (4), 605–612. https://doi.org/10.1111/j.1365-3091.1985.tb00474.x.

Boait, F.C., White, N.J., Bickle, M.J., Chadwick, R.A., Neufeld, J.A., Huppert, H.E., 2012. Spatial and temporal evolution of injected CO2 at the Sleipner Field, North Sea. J. Geophys. Res. Solid Earth 117 (B3). https://doi.org/10.1029/2011JB008603.

Boles, J.R., Clark, J.F., Leifer, I., Washburn, L., 2001. Temporal variation in natural methane seep rate due to tides, Coal Oil Point area, California. J. Geophys. Res. 106 (C11) https://doi.org/10.1029/2000JC000774, 27,077–27,086.

Böttner, C., Berndt, C., Reinardy, B.T.I., Geersen, J., Karstens, J., Bull, J.M., Callow, B.J., Lichtschlag, A., Schmidt, M., Elger, J., Schramm, B., Haeckel, M., 2019. Pockmarks in the Witch Ground Basin, Central North Sea. Geochem. Geophys. Geosystems 20, 1698–1719. https://doi.org/10.1029/2018gc008068.

Böttner, C., Callow, B.J., Schramm, B., Gross, F., Geersen, J., Schmidt, M., Vasilev, A., Petsinski, P., & Berndt, C., (in review). Focused methane migration formed pipe structures in permeable sandstones: Insights from UAV-based digital outcrop analysis in Varna, Bulgaria.

Bouchaala, F., Ali, M.Y., Matsushima, J., Bouzide, Y., Takam Takougang, E.M., Mohamed, A., Sultan, A., 2019. Azimuthal investigation of compressional seismic-wave attenuation in a fractured reservoir. Geophysics 84, B437–B446. https://doi.org/10.1190/geo2019-0079.1.

Boudreau, B.P., Algar, C., Johnson, B.D., Croudace, I., Reed, A., Furukawa, Y., Dorgan, K. M., Jumars, P.A., Grader, A.S., Gardiner, B.S., 2005. Bubble growth and rise in soft sediments. Geology 33, 517–520. https://doi.org/10.1130/G21259.1.

Bouma, A.H., Boerma, J.A.K., 1968. Vertical disturbances in piston cores. Mar. Geol. 6 (3), 231–241. https://doi.org/10.1016/0025-3227(68)90032-7.

Brossier, R., Operto, S., Virieux, J., 2015. Velocity model building from seismic reflection data by full-waveform inversion. Geophys. Prospect. 63 (2), 354–367. https://doi.org/10.1111/1365-2478.12190.

Bull, J.M., 2017. Cruise Report – RRS James Cook JC152: CHIMNEY - Characterisation of Major Overburden Pathways Above Sub-seafloor CO_2 Storage Reservoirs in the North Sea. Scanner and Challenger Pockmark Complexes. https://eprints.soton.ac.uk/420257/.

Bull, J.M., Berndt, C.B., Minshull, T.M., Henstock, T., Bayrakci, G., Gehrmann, R., Provenzano, G., Bottner, C., Schramm, B., Callow, B., Chapman, M., Birinci, H., Yilo, N., Dewar, M., Chen, B., Saleem, U., Marin-Moreno, H., Lichtschlag, A., Falcon-Suarez, I., Roche, B., James, R.H., Connelly, D.P., Matter, J., Elger, J., Karstens, J., Best, A.I., 2018. Constraining leakage pathways through the overburden Above sub-seafloor CO_2 storage reservoirs. 14th Greenhouse Gas Control Technologies Conference Melbourne 21-26 October 2018 (GHGT-14).

Bünz, S., Mienert, J., Berndt, C., 2003. Geological controls on the Storegga gas-hydrate system of the mid-Norwegian continental margin. Earth Planet. Sci. Lett. 209 (3–4), 291–307. https://doi.org/10.1016/S0012-821X(03)00097-9.

Bünz, S., Polyanov, S., Vadakkepuliyambatta, S., Consolaro, C., Mienert, J., 2012. Active gas venting through hydrate-bearing sediments on the Vestnesa Ridge, offshore W-Svalbard. Mar. Geol. 332, 189–197. https://doi.org/10.1016/j.margeo.2012.09.012.

Cartwright, J., 2007. The impact of 3D seismic data on the understanding of compaction, fluid flow and diagenesis in sedimentary basins. J. Geol. Soc. 164 (5), 881–893. https://doi.org/10.1144/0016-76492006-143.

Cartwright, J., Huuse, M., 2005. 3D seismic technology: the geological 'Hubble'. Basin Res. 17 (1), 1–20. https://doi.org/10.1111/j.1365-2117.2005.00252.x.

Cartwright, J., Santamarina, C., 2015. Seismic characteristics of fluid escape pipes in sedimentary basins: implications for pipe genesis. Mar. Pet. Geol. 65, 126–140. https://doi.org/10.1016/j.marpetgeo.2015.03.023.

Cartwright, J., Huuse, M., Aplin, A., 2007. Seal bypass systems. Bull. 91, 1141–1166. https://doi.org/10.1306/04090705181.

Cathles, L.M., Su, Z., Chen, D., 2010. The physics of gas chimney and pockmark formation, with implications for assessment of seafloor hazards and gas sequestration. Mar. Pet. Geol. 27 (1), 82–91. https://doi.org/10.1016/j.marpetgeo.2009.09.010.

Cevatoglu, M., Bull, J.M., Vardy, M.E., Gernon, T.M., Wright, I.C., Long, D., 2015. Gas migration pathways, controlling mechanisms and changes in sediment acoustic properties observed in a controlled sub-seabed CO 2 release experiment. Int. J. Greenh. Gas Control 38, 26–43. https://doi.org/10.1016/j.ijggc.2015.03.005.

Chadwick, R.A., Arts, R., Eiken, O., Kirby, G.A., Lindeberg, E., Zweigel, P., 2004. 4D seismic imaging of an injected C02 plume at the Sleipner Field, Central North Sea. Geol. Soc. London Mem. 29 (1), 311–320. https://doi.org/10.1144/GSL.MEM.2004.029.01.29.

Chadwick, R.A., Williams, G.A., Falcon-Suarez, I., 2019. Forensic mapping of seismic velocity heterogeneity in a CO2 layer at the Sleipner CO2 storage operation, North Sea, using time-lapse seismics. Int. J. Greenh. Gas Control 90, 102793 https://doi.org/10.1016/j.ijggc.2019.102793.

Chapman, M., 2003. Frequency-dependent anisotropy due to meso-scale fractures in the presence of equant porosity. Geophys. Prospect. 51 (5), 369–379. https://doi.org/10.1046/j.1365-2478.2003.00384.x.

Chapman, M., 2009. Modeling the effect of multiple sets of mesoscale fractures in porous rock on frequency-dependent anisotropy. Geophysics 74 (6), D97–D103. https://doi.org/10.1190/1.3204779.

Cheeseman, S.J., Edwards, R.N., Chave, A.D., 1987. On the theory of sea floor conductivity mapping using transient electromagnetic systems. Geophysics 52, 204–217. https://doi.org/10.1190/1.1442296.

Clay, S., Vardy, M., 2018. Optimisation of source and receiver geometry for ultra High frequency seismic data. In: European Association of Geoscientists & Engineers3rd Applied Shallow Marine Geophysics Conference, Vol. 2018, pp. 1–5. https://doi.org/10.3997/2214-4609.201802673. No. 1.

Clayton, C.J., Dando, P.R., 1996. Comparison of seepage and seal leakage rates. In: Schumacher, D., Abrams, M.A. (Eds.), Hydrocarbon Migration and Its Near-Surface Expression. in Outgrowth of the AAPG Hedberg Research Conference. American Association of Petroleum Geologists Memoir. Vancouver, British Columbia, April 24-28, 1994 (No. 66). AAPG.

Cole, D., Stewart, S.A., Cartwright, J.A., 2000. Giant irregular pockmark craters in the palaeogene of the Outer Moray Firth Basin, UK North Sea. Mar. Pet. Geol. 17, 563–577. https://doi.org/10.1016/S0264-8172(00)00013-1.

Constable, S., 2010. Ten years of marine CSEM for hydrocarbon exploration. Geophysics 75 (5), 75A67–75A81. https://doi.org/10.1190/1.3483451.

Constable, S., 2013. Review paper: instrumentation for marine magnetotelluric and controlled source electromagnetic sounding. Geophys. Prospect. 61 (s1), 505–532. https://doi.org/10.1111/j.1365-2478.2012.01117.x.

Constable, S.C., Parker, R.L., Constable, C.G., 1987. Occam's inversion: a practical algorithm for generating smooth models from electromagnetic sounding data. Geophysics 52 (3), 289–300. https://doi.org/10.1190/1.1442303.

Constable, S., Kannberg, P.K., Weitemeyer, K., 2016. Vulcan: a deep-towed CSEM receiver. Geochem. Geophys. Geosystems 17 (3), 1042–1064. https://doi.org/10.1002/2015GC006174.

Crain, E.R., 2010. Crain's Petrophysical Handbook, Spectrum 2000 Mindware. Rocky Mountain House, AB, p. 2019. https://www.spec2000.net.

Crampin, S., 1985. Evaluation of anisotropy by shear-wave splitting. Geophysics 50 (1), 142–152. https://doi.org/10.1190/1.1441824.

Davy, R.G., Morgan, J.V., Minshull, T.A., Bayrakci, G., Bull, J.M., Klaeschen, D., Reston, T.J., Sawyer, D.S., Lymer, G., Cresswell, D., 2018. Resolving the fine-scale velocity structure of continental hyperextension at the Deep Galicia Margin using full-waveform inversion. Geophys. J. Int. 212 (1), 244–263. https://doi.org/10.1093/gji/ggx415.

De Boever, E., Swennen, R., Dimitrov, L., 2006a. Lower Eocene carbonate cemented chimneys (Varna, NE Bulgaria): Formation mechanisms and the (a) biological mediation of chimney growth? Sediment. Geol. 185 (3–4), 159–173. https://doi.org/10.1016/j.sedgeo.2005.12.010.

De Boever, E., Swennen, R., Dimitrov, L., 2006b. Lower Eocene carbonate-cemented "chimney" structures (Varna, Bulgaria)—control of seepage rates on their formation and stable isotopic signature. J. Geochem. Explor. 89 (1–3), 78–82. https://doi.org/10.1016/j.gexplo.2005.11.028.

Dean, M., Tucker, O., 2017. A risk-based framework for Measurement, Monitoring and Verification (MMV) of the Goldeneye storage complex for the Peterhead CCS project, UK. Int. J. Greenh. Gas Control 61, 1–15. https://doi.org/10.1016/j.ijggc.2017.03.014.

Dean, M., Tucker, O.D., Strijbos, F.P.L., de Jong, R.A.M., Marshall, J., Goswami, R., 2015. Characterisation and monitoring of the goldeneye CO2 storage site. 77th EAGE Conference and Exhibition 2015. https://doi.org/10.3997/2214-4609.201412719.

Deusner, C., Gupta, S., Kossel, E., Freise, M., Anbergen, H., Wille, T., Bigalke, N., Haeckel, M., 2016. The role of high-pressure flow-through experiments for evaluating the mechanical behaviour of gas hydrate-bearing soils. Energy Geotechnics 437–443. https://doi.org/10.1201/b21938-70.

Dickens, G., Koelling, M., Smith, D., Schnieders, L., IODP Exp. 302 Scientists, 2007. Rhizon sampling of pore waters on scientific drilling expeditions: an example from the IODP Expedition 302, Arctic Coring Expedition (ACEX). IODP Sci. Drill. 4, 22–25. https://doi.org/10.2204/iodp.sd.4.08.2007.

Domenico, S.N., 1977. Elastic properties of unconsolidated porous sand reservoirs. Geophysics 42 (7), 1339–1368. https://doi.org/10.1190/1.1440797.

Dunn, R.A., Toomey, D.R., 2001. Crack-induced seismic anisotropy in the oceanic crust across the East Pacific Rise (9 30′ N). Earth Planet. Sci. Lett. 189 (1–2), 9–17. https://doi.org/10.1016/S0012-821X(01)00353-3.

Dunn, R.A., Lekić, V., Detrick, R.S., Toomey, D.R., 2005. Three-dimensional seismic structure of the Mid-Atlantic Ridge (35 N): evidence for focused melt supply and lower crustal dike injection. J. Geophys. Res. Solid Earth 110 (B9). https://doi.org/10.1029/2004JB003473.

Edwards, R.N., 1988. Two-dimensional modeling of a towed in-line electric dipole-dipole seafloor electromagnetic system: the optimum time delay or frequency for target resolution. Geophysics 53 (6), 846–853. https://doi.org/10.1190/1.1442519.

Edwards, R.N., 1997. On the resource evaluation of marine gas hydrate deposits using sea-floor transient electric dipole-dipole methods. Geophysics 62 (1), 63–74. https://doi.org/10.1190/1.1444146.

Edwards, R.N., 2005. Marine controlled source electromagnetics: principles, methodologies, future commercial applications. In: Surveys in Geophysics, 26. Springer, Berlin, Heidelberg, New York, pp. 675–700. https://doi.org/10.1007/s10712-005-1830-3.

Eiken, O., 2019. Twenty years of monitoring CO2 injection at Sleipner. In: Davis, T.L., Landrø, M., Wilson, M. (Eds.), Geophysics and Geosequestration. Cambridge University Press, pp. 209–234.

Ellingsrud, S., Eidesmo, T., Johansen, S., Sinha, M.C., MacGregor, L.M., Constable, S., 2002. Remote sensing of hydrocarbon layers by seabed logging (SBL): results from a cruise offshore Angola. Lead. Edge 21 (10), 972–982. https://doi.org/10.1190/1.1518433.

EU CCS Directive on Geological Storage of Carbon Dioxide, 2009. Directive 2009/31/EC of the European Parliament and of the Council. Off. J. Eur. Union. L 140/114 EN. https://eur-lex.europa.eu/LexUriServ/LexUriServ.do?uri=OJ:L:2009:140:0114:0135:EN:PDF.

Falcon-Suarez, I., North, L., Amalokwu, K., Best, A., 2016. Integrated geophysical and hydromechanical assessment for CO2 storage: shallow low permeable reservoir sandstones. Geophys. Prospect. 64, 828–847. https://doi.org/10.1111/1365-2478.12396.

Fader, G.B.J., 1997. The Effects of Shallow Gas on Seismic Reflection Profiles. In: Davies, T.A., Bell, T., Cooper, A., Josenhans, H., Polyak, L., Solheim, A., Stoker, M.S., Stravers, J.A. (Eds.), Glaciated Continental Margins. Springer, pp. 29–30.

Falcon-Suarez, I.H., Amalokwu, K., Delgado-Martin, J., Callow, B., Robert, K., North, L., Sahoo, S.K., Best, A.I., 2019. Comparison of stress-dependent geophysical, hydraulic and mechanical properties of synthetic and natural sandstones for reservoir

characterization and monitoring studies. Geophys. Prospect. 67 (4), 784–803. https://doi.org/10.1111/1365-2478.12699.

Falcon-Suarez, I., Marín-Moreno, H., Browning, F., Lichtschlag, A., Robert, K., North, L. J., Best, A.I., 2017. Experimental assessment of pore fluid distribution and geomechanical changes in saline sandstone reservoirs during and after CO2 injection. Int. J. Greenh. Gas Control. 63, 356–369. https://doi.org/10.1016/j.ijggc.2017.06.019.

Falcon-Suarez, I., Papageorgiou, G., Chadwick, A., North, L., Best, A., Chapman, M., 2018. CO2-brine flow-through on an Utsira Sand core sample: experimental and modelling. Implications for the Sleipner storage field. Int. J. Greenh. Gas Control 68, 236–246. https://doi.org/10.1016/j.ijggc.2017.11.019.

Fauria, K.E., Rempel, A.W., 2011. Gas invasion into water-saturated, unconsolidated porous media: implications for gas hydrate reservoirs. Earth Planet. Sci. Lett. 312 (1–2), 188–193. https://doi.org/10.1016/j.epsl.2011.09.042.

Flohr, A., Schapp, A., Achterberg, E.P., Alendal, G., Arundell, M., Berndt, C., Blackford, J., Böttner, C., Borisov, S.M., Brown, R., Bull, J.M., Carter, L., Chen, B., Dale, A.W., de Beer, D., Dean, M., Deusner, C., Dewar, M., Durden, J.M., Elsen, S., Esposito, M., Faggetter, M., Fischer, J.P., Gana, A., Gros, J., Haeckel, M., Hanz, R., Holtappels, M., Hosking, B., Huvenne, V.A.I., James, R.H., Koopmans, D., Kossel, E., Leighton, T.G., Li, J., Lichtschlag, A., Linke, P., Loucaides, S., Martínez-Cabanas, M., Matter, J.M., Mesher, T., Monk, S., Mowlem, M., Oleynik, A., Papadimitriou, S., Paxton, D., Pearce, C.R., Peel, K., Roche, B., Ruhl, H.A., Saleem, U., Sands, C., Saw, K., Schmidt, M., Sommer, S., Strong, J.A., Triest, J., Ungerböck, B., Walk, J., White, P., Widdicombe, S., Wilson, R.E., Wright, H., Wyatt, J., Connelly, D., 2021. Towards improved monitoring of offshore carbon storage: a real-world field experiment detecting a controlled sub-seafloor CO2 release. Int. J. Greenhouse Gas Control.

Frey, S.E., Gingras, M.K., Dashtgard, S.E., 2009. Experimental studies of gas-escape and water-escape structures: mechanisms and morphologies. J. Sediment. Res. 79 (11), 808–816. https://doi.org/10.2110/jsr.2009.087.

Furre, A.-K., Meneguloz, R., Ringrose, P., Kassold, S., 2019a. Building confidence in CCS: from sleipner to the northern lights project. First Break. 37 (7), 81–87. https://doi.org/10.3997/1365-2397.n0038.

Furre, A., Ringrose, P., Santi, A.C., 2019b. In: 81st EAGE Conference and Exhibition 2019Observing the invisible – CO2 feeder chimneys on seismic time-lapse data, Volume 2019, pp. 1–5. https://doi.org/10.3997/2214-4609.201901646.

Gafeira, J., Long, D., 2015. Geological Investigation of Pockmarks in the Scanner Pockmark SCI Area. JNCC Report No 570. JNCC Peterborough. http://data.jncc.gov.uk/data/290b95b7-fcfc-4c76-8780-8714329dcf0c/JNCC-Report-570-FINAL-WEB.pdf.

Gay, A., Lopez, M., Berndt, C., Séranne, M., 2007. Geological controls on focused fluid flow associated with seafloor seeps in the Lower Congo Basin. Mar. Geol. 244, 68–92. https://doi.org/10.1016/j.margeo.2007.06.003.

GEBCO, 2019. The GEBCO_2019 Grid - a Continuous Terrain Model of the Global Oceans and Land. British Oceanographic Data Centre, National Oceanography Centre, NERC, UK https://doi.org/10/c33m.

Gehrmann, R.A.S., North, L.J., Graber, S., Szitkar, F., Petersen, S., Minshull, T.A., Murton, B.J., 2019. Marine mineral exploration with controlled-source electromagnetics at the TAG hydrothermal field, 26N Mid-Atlantic Ridge. Geophys. Res. Lett. 46 (11), 5808–5816. https://doi.org/10.1029/2019GL082928.

Gehrmann, R.A.S., Provenzano, G., Böttner, C., Marin-Moreno, H., Bayrakci, G., Tan, Y. Y., Yilo, N.K., Djanni, A.T., Weitemeyer, K.A., Minshull, T.A., Bull, J.M., Karstens, J., Berndt, C., (this volume, in review). Porosity and free gas estimates from controlled source electromagnetic data at the Scanner Pockmark in the North Sea. Int. J. Greenh. Gas Control.

Global CCS Institute, 2019. The Global Status of CCS: 2019, Melbourne, Australia. https://www.globalccsinstitute.com/wpcontent/uploads/2019/12/GCC_GLOBAL_STATUS_REPORT_2019.pdf.

Górszczyk, A., Operto, S., Malinowski, M., 2017. Toward a robust workflow for deep crustal imaging by FWI of OBS data: the eastern Nankai Trough revisited. J. Geophys. Res. Solid Earth 122 (6), 4601–4630. https://doi.org/10.1002/2016JB013891.

Goswami, B.K., Weitemeyer, K.A., Minshull, T.A., Sinha, M.C., Westbrook, G.K., Chabert, A., Henstock, T., Ker, S., 2015. A joint electromagnetic and seismic study of an active pockmark within the hydrate stability field at the Vestnesa Ridge, West Svalbard margin. J. Geophys. Res. Solid Earth 120 (10), 6797–6822. https://doi.org/10.1002/2015JB012344.

Graber, K.K., Pollard, E., Jonasson, B., Schulte, E., 2002. Overview of Ocean Drilling Program Engineering Tools and Hardware. https://doi.org/10.2973/odp.tn.31.2002.

Haacke, R.R., Westbrook, G.K., 2006. A fast, robust method for detecting and characterizing azimuthal anisotropy with marine PS converted waves, and its application to the west Svalbard continental slope. Geophys. J. Int. 167 (3), 1402–1412. https://doi.org/10.1111/j.1365-246X.2006.03186.x.

Haacke, R.R., Westbrook, G.K., Peacock, S., 2009. Layer stripping of shear-wave splitting in marine PS waves. Geophys. J. Int. 176 (3), 782–804. https://doi.org/10.1111/j.1365-246X.2008.04060.x.

Harrington, R.M., Brodsky, E.E., 2007. Volcanic hybrid earthquakes that are brittle-failure events. Geophys. Res. Lett. 34 (6) https://doi.org/10.1029/2006GL028714.

Harris, P.E., Du, Z., MacGregor, L., Olsen, W., Shu, R., Cooper, R., 2009. Joint interpretation of seismic and CSEM data using well log constraints: an example from the Luva Field. First Break. 27 (5) https://doi.org/0.3997/1365-2397.27.1299.28932.

Hindle, A.D., 1997. Petroleum migration pathways and charge concentration: a three-dimensional model. AAPG Bulletin 81 (9), 1451–1481. https://doi.org/10.1306/3B05BB1E-172A-11D7-8645000102C1865D.

Hoversten, G.M., Cassassuce, G., Gasperikova, E., Newman, G.A., Chen, J., Rubein, Y., Hou, Z., Vasco, D., 2006. Direct reservoir parameter estimation using joint inversion of marine seismic AVA and CSEM data. Geophysics 71 (3), C1–C13. https://doi.org/10.1190/1.2194510.

Hovland, M., Sommerville, J.H., 1985. Characteristics of two natural gas seepages in the North Sea. Mar. Pet. Geol. 2 (4), 319–326. https://doi.org/10.1016/0264-8172(85)90027-3.

Hovland, M., Heggland, R., De Vries, M.H., Tjelta, T.I., 2010. Unit-pockmarks and their potential significance for predicting fluid flow. Mar. Pet. Geol. 27, 1190–1199. https://doi.org/10.1016/j.marpetgeo.2010.02.005.

Hudson, J.A., 1981. Wave speeds and attenuation of elastic waves in material containing cracks. Geophys. J. Int. 64 (1), 133–150. https://doi.org/10.1111/j.1365-246X.1981.tb02662.x.

Hurst, A., Scott, A., Vigorito, M., 2011. Physical characteristics of sand injectites. Earth. Rev. 106 (3–4), 215–246. https://doi.org/10.1016/j.earscirev.2011.02.004.

Hustoft, S., Bünz, S., Mienert, J., 2010. Three-dimensional seismic analysis of the morphology and spatial distribution of chimneys beneath the Nyegga pockmark field, offshore mid-Norway. Basin Res. 22 (4), 465–480. https://doi.org/10.1111/j.1365-2117.2010.00486.x.

Huuse, M., Shoulders, S.J., Netoff, D.I., Cartwright, J., 2005. Giant sandstone pipes record basin-scale liquefaction of buried dune sands in the Middle Jurassic of SE Utah. Terra Nova 17 (1), 80–85. https://doi.org/10.1111/j.1365-3121.2004.00587.x.

Huuse, M., Jackson, C.A.L., Van Rensbergen, P., Davies, R.J., Flemings, P.B., Dixon, R.J., 2010. Subsurface sediment remobilization and fluid flow in sedimentary basins: an overview. Basin Res. 22 (4), 342–360. https://doi.org/10.1111/j.1365-2117.2010.00482.x.

IPCC, 2005. Carbon Dioxide Capture and Storage. Cambridge University Press, Cambridge, England. https://www.ipcc.ch/report/carbon-dioxide-capture-and-storage/.

IPCC, 2014. In: Core Writing Team, Pachauri, R.K., Meyer, L.A. (Eds.), Climate Change 2014: Synthesis Report. Contribution of Working Groups I, II and III to the Fifth Assessment Report of the Intergovernmental Panel on Climate Change. IPCC, Geneva, Switzerland, p. 151. https://epic.awi.de/id/eprint/37530/1/IPCC_AR5_SYR_Final.pdf.

Jakobsen, M., Chapman, M., 2009. Unified theory of global flow and squirt flow in cracked porous media. Geophysics 74 (2), WA65–WA76. https://doi.org/10.1190/1.3078404.

Jannane, M., Beydoun, W., Crase, E., Cao, D., Koren, Z., Landa, E., Mendes, M., Pica, A., Noble, M., Rotes, G., Singh, S., Snieder, R., Tarantola, A., Trezeguet, D., Xie, M., 1989. Wavelengths of earth structures that can be resolved from seismic reflection data. Geophysics 54 (7), 906–910. https://doi.org/10.1190/1.1442719.

Jin, Z., Chapman, M., Papageorgiou, G., 2018. Frequency-dependent anisotropy in a partially saturated fractured rock. Geophys. J. Int. 215 (3), 1985–1998. https://doi.org/10.1093/gji/ggy399.

Johnston, D.H., 2013. Practical applications of time-lapse seismic data. Society of Exploration Geophysicists.

Judd, A., Hovland, M., 2009. Seabed Fluid Flow: the Impact on Geology, Biology and the Marine Environment. Cambridge University Press. https://doi.org/10.1017/CBO9780511535918.

Judd, A., Long, D., Sankey, M., 1994. Pockmark formation and activity, UK block 15/25, North Sea. Bull. Geol. Soc. Denmark 41, 34–49.

Kallweit, R.S., Wood, L.C., 1982. The limits of resolution of zero-phase wavelets. Geophysics 47 (7), 1035–1046. https://doi.org/10.1190/1.1441367.

Karstens, J., Berndt, C., 2015. Seismic chimneys in the Southern Viking Graben – implications for palaeo fluid migration and overpressure evolution. Earth Planet. Sci. Lett. 412, 88–100. https://doi.org/10.1016/j.epsl.2014.12.017.

Karstens, J., Böttner, C., Edwards, M., Falcon-Suarez, I., Flohr, A., James, R., Lichtschlag, A., Maicher, D., Pheasant, I., Roche, B., Schramm, B., Wilson, M., 2019. RV MARIA S. MERIAN Cruise Report MSM78-PERMO2, Edinburgh–Edinburgh (UK), 16.10.-25.10.2018. https://doi.org/10.3289/geomar_rep_ns_48_2019.

Kim, Y., Nakata, N., 2018. Geophysical inversion versus machine learning in inverse problems. Lead. Edge 37 (12), 894–901. https://doi.org/10.1190/tle37120894.1.

Kong, Q., Trugman, D.T., Ross, Z.E., Bianco, M.J., Meade, B.J., Gerstoft, P., 2019. Machine Learning in Seismology: Turning Data into Insights. Seismological Research Letters 90 (1), 3–14. https://doi.org/10.1785/0220180259.

Lacoss, R., Kelly, E., Toksöz, M., 1969. Estimation of seismic noise structure using arrays. Geophysics 34, 21–38. https://doi.org/10.1190/1.1439995.

Landrø, M., Solheim, O.A., Hilde, E., Ekren, B.O., Stronen, L.K., 1999. The Gullfaks 4D seismic study. Pet. Geosci. 5 (3), 213–226. https://doi.org/10.1144/petgeo.5.3.213.

Latter, J.H., 1981. Volcanic earthquakes, and their relationship to eruptions at Ruapehu and Ngauruhoe volcanoes. J. Volcanol. Geotherm. Res. 9 (4), 293–309. https://doi.org/10.1016/0377-0273(81)90041-X.

Lee, M.W., 2004. Elastic velocities of partially gas-saturated unconsolidated sediments. Mar. Pet. Geol. 21 (6), 641–650. https://doi.org/10.1016/j.marpetgeo.2003.12.004.

Li, X.Y., 1997. Fractured reservoir delineation using multicomponent seismic data. Geophys. Prospect. 45 (1), 39–64. https://doi.org/10.1046/j.1365-2478.1997.3200262.x.

Li, J., Roche, B., Bull, J.M., White, P.R., Leighton, T.G., Provenzano, G., Dewar, M., Henstock, T., 2020. Broadband acoustic inversion for gas flux quantication - application to a methane plume at Scanner Pockmark, central North Sea. J. Geophys. Res. Oceans 125 (9). https://doi.org/10.1029/2020JC016360.

Lin, L., Hsu, H., Liu, C., et al., 2019. Marine 3D seismic volumes from 2D seismic survey with large streamer feathering. Mar. Geophys. Res. 40, 619–633. https://doi.org/10.1007/s11001-019-09391-9.

Linke, P., Haeckel, M., 2018. RV POSEIDON Cruise Report POS518: Baseline Study for the Environmental Monitoring of Subseafloor CO2 Storage Operations, Leg 2: Bremerhaven – Kiel (Germany) 12.10.-28.10.2017. https://doi.org/10.3289/GEOMAR_REP_NS_40_2018.

Liu, E., Hudson, J.A., Pointer, T., 2000. Equivalent medium representation of fractured rock. J. Geophys. Res. Solid Earth 105 (B2), 2981–3000. https://doi.org/10.1029/1999JB900306.

Liu, J., Haeckel, M., Rutqvist, J., Wang, S., Yan, W., 2019. The mechanism of methane gas migration through the gas hydrate stability zone: insights from numerical simulations. J. Geophys. Res. 124, 4399–4427. https://doi.org/10.1029/2019JB017417.

Løseth, H., Gading, M., Wensaas, L., 2009. Hydrocarbon leakage interpreted on seismic data. Mar. Pet. Geol. 26 (7), 1304–1319. https://doi.org/10.1016/j.marpetgeo.2008.09.008.

Løseth, H., Wensaas, L., Arntsen, B., Hanken, N.-M., Basire, C., Graue, K., 2011. 1000 m long gas blow-out pipes. Mar. Pet. Geol. 28, 1047–1060. https://doi.org/10.1016/j.marpetgeo.2010.10.001.

Lowe, D.R., 1975. Water escape structures in coarse-grained sediments. Sedimentology 22 (2), 157–204. https://doi.org/10.1111/j.1365-3091.1975.tb00290.x.

Lumley, D., 2010. 4D seismic monitoring of CO2 sequestration. Lead. Edge 29 (2), 150–155. https://doi.org/10.1190/1.3304817.

Marín-Moreno, H., Bull, J.M., Matter, J., Sanderson, D.J., Roche, B., 2019. Reactive transport modeling insights into CO2 migration through sub-vertical fluid flow structures. Int. J. Greenh. Gas Control. 86, 82–92. https://doi.org/10.1016/j.ijggc.2019.04.018.

Maultzsch, S., Chapman, M., Liu, E., Li, X.Y., 2003. Modelling frequency-dependent seismic anisotropy in fluid-saturated rock with aligned fractures: implication of fracture size estimation from anisotropic measurements. Geophys. Prospect. 51 (5), 381–392. https://doi.org/10.1046/j.1365-2478.2003.00386.x.

Maultzsch, S., Chapman, M., Liu, E., Li, X.Y., 2007. Modelling and analysis of attenuation anisotropy in multi-azimuth VSP data from the Clair field. Geophys. Prospect. 55 (5), 627–642. https://doi.org/10.1111/j.1365-2478.2007.00645.x.

Mavko, G., Mukerji, T., Dvorkin, J., 2009. The Rock Physics Handbook: Tools for Seismic Analysis of Porous Media. Cambridge University Press.

McDermott, C., Kolditz, O., 2006. Geomechanical model for fracture deformation under hydraulic, mechanical and thermal loads. Hydrogeol. J. 14 (4), 485–498. https://doi.org/10.1007/s10040-005-0455-4.

Minnaert, M., 1933. XVI. On musical air-bubbles and the sounds of running water. The London, Edinburgh, and Dublin. Philos. Mag. J. Sci. 16 (104), 235–248. https://doi.org/10.1080/14786443309462277.

Minshull, T.A., Sinha, M.C., Peirce, C., 2005. Multi-disciplinary, sub-seabed geophysical imaging – a new pool of 28 seafloor instruments in use by the United Kingdom Ocean Bottom Instrument Consortium. Sea Technol. 46 (10), 27–31. http://eprints.soton.ac.uk/id/eprint/18172.

Morgan, J., Warner, M., Bell, R., Ashley, J., Barnes, D., Little, R., Roele, K., Jones, C., 2013. Next-generation seismic experiments: wide-angle, multi-azimuth, three-dimensional, full-waveform inversion. Geophys. J. Int. 195 (3), 1657–1678. https://doi.org/10.1093/gji/ggt345.

Moss, J.L., Cartwright, J., 2010a. 3D seismic expression of km-scale fluid escape pipes from offshore Namibia. Basin Res. 22 (4), 481–501. https://doi.org/10.1111/j.1365-2117.2010.00461.x.

Moss, J.L., Cartwright, J., 2010b. The spatial and temporal distribution of pipe formation, offshore Namibia. Mar. Pet. Geol. 27 (6), 1216–1234. https://doi.org/10.1016/j.marpetgeo.2009.12.013.

Mueller, M.C., 1992. Using shear waves to predict lateral variability in vertical fracture intensity. Lead. Edge 11 (2), 29–35. https://doi.org/10.1190/1.1436870.

Muñoz-Ibáñez, A., Falcon-Suarez, I.H., Marín-Moreno, H., Martín, J.D., Mackin, P., 2019. Transport properties of saline CO2 storage reservoirs with unconnected fractures from brine-CO2 flow-through tests. J. Pet. Sci. Eng., 106551 https://doi.org/10.1016/j.petrol.2019.106551.

Myer, D., Constable, S., Key, K., 2011. Broad-band waveforms and robust processing for marine CSEM surveys. Geophys. J. Int. 184 (2), 689–698. https://doi.org/10.1111/j.1365-246X.2010.04887.x.

Naif, S., Key, K., Constable, S., Evans, R.L., 2015. Water-rich bending faults at the middle america trench. Geochem. Geophys. Geosystems 16 (8), 2582–2597. https://doi.org/10.1002/2015GC005927.

Nichols, R.J., Sparks, R.S.J., Wilson, C.J.N., 1994. Experimental studies of the fluidization of layered sediments and the formation of fluid escape structures. Sedimentology 41 (2), 233–253. https://doi.org/10.1111/j.1365-3091.1994.tb01403.x.

Ostrander, W., 1984. Plane-wave reflection coefficients for gas sands at nonnormal angles of incidence. Geophysics 49 (10), 1637–1648. https://doi.org/10.1190/1.1441571.

Ottesen, D., Dowdeswell, J.A., Bugge, T., 2014. Morphology, sedimentary infill and depositional environments of the Early Quaternary North Sea Basin (56–62 N). Mar. Pet. Geol. 56, 123–146. https://doi.org/10.1016/j.marpetgeo.2014.04.007.

Palacky, G.V., 1988. Resistivity characteristics of geologic targets. In: Nabighian, Misac N. (Ed.), Electromagnetic Methods in Applied Geophysics, volume 1. Society of Exploration Geophysicists, pp. 52–129. https://doi.org/10.1190/1.9781560802631 chapter 3.

Panieri, G., Bünz, S., Fornari, D.J., Escartin, J., Serov, P., Jansson, P., Torres, M.E., Johnson, J.E., Hong, W., Sauer, S., Garcia, R., 2017. An integrated view of the methane system in the pockmarks at Vestnesa Ridge, 79 N. Mar. Geol. 390, 282–300. https://doi.org/10.1016/j.margeo.2017.06.006.

Pape, T., Hohnberg, H.-J., Wunsch, D., Anders, E., Freudenthal, T., Huhn, K., Bohrmann, G., 2017. Design and deployment of autoclave pressure vessels for the

portable deep-sea drill rig MeBo (Meeresboden-Bohrgerät). Sci. Drill. 23, 29–37. https://doi.org/10.5194/sd-23-29-2017.

Petersen, C.J., Bünz, S., Hustoft, S., Mienert, J., Klaeschen, D., 2010. High-resolution P-Cable 3D seismic imaging of gas chimney structures in gas hydrated sediments of an Arctic sediment drift. Mar. Pet. Geol. 27 (9), 1981–1994. https://doi.org/10.1016/j.marpetgeo.2010.06.006.

Picozzi, M., Parolai, S., Bindi, D., 2010. Deblurring of frequency–wavenumber images from small-scale seismic arrays. Geophys. J. Int. 181 (1), 357–368. https://doi.org/10.1111/j.1365-246X.2009.04471.x.

Planke, S., Eriksen, F.N., Berndt, C., Mienert, J., Masson, D.G., 2009. P-Cable high-resolution seismic. Oceanography 22 (1), 85. https://doi.org/10.5670/oceanog.2009.09.

Plaza-Faverola, A., Bünz, S., Mienert, J., 2010. Fluid distributions inferred from P-wave velocity and reflection seismic amplitude anomalies beneath the Nyegga pockmark field of the mid-Norwegian margin. Mar. Pet. Geol. 27 (1), 46–60. https://doi.org/10.1016/j.marpetgeo.2009.07.007.

Plaza-Faverola, A., Bünz, S., Mienert, J., 2011. Repeated fluid expulsion through sub-seabed chimneys offshore Norway in response to glacial cycles. Earth Planet. Sci. Lett. 305 (3–4), 297–308. https://doi.org/10.1016/j.epsl.2011.03.001.

Plaza-Faverola, A., Vadakkepuliyambatta, S., Hong, W.L., Mienert, J., Bünz, S., Chand, S., Greinert, J., 2017. Bottom-simulating reflector dynamics at Arctic thermogenic gas provinces: an example from Vestnesa Ridge, offshore west Svalbard. J. Geophys. Res. Solid Earth 122, 4089–4105. https://doi.org/10.1002/2016jb013761.

Plaza-Faverola, A., Bünz, S., Johnson, J.E., Chand, S., Knies, J., Mienert, J., Franek, P., 2015. Role of tectonic stress in seepage evolution along the gas hydrate-charged Vestnesa Ridge, Fram Strait. Geophys. Res. Lett. 42 (3), 733–742. https://doi.org/10.1002/2014GL062474.

Prieux, V., Brossier, R., Operto, S., Virieux, J., 2013. Multiparameter full waveform inversion of multicomponent ocean-bottom-cable data from the Valhall field. Part 1: imaging compressional wave speed, density and attenuation. Geophys. J. Int. 194 (3), 1640–1664. https://doi.org/10.1093/gji/ggt177.

Provenzano, G., Vardy, M.E., Henstock, T.J., 2018. Decimetric-resolution stochastic inversion of shallow marine seismic reflection data: dedicated strategy and application to a geohazard case study. Geophys. J. Int. 214 (3), 1683–1700. https://doi.org/10.1093/gji/ggy221.

Räss, L., Simon, N.S.C., Podladchikov, Y.Y., 2018. Spontaneous formation of fluid escape pipes from subsurface reservoirs. Sci. Rep. 8, 11116. https://doi.org/10.1038/s41598-018-29485-5.

Reinardy, B.T., Hjelstuen, B.O., Sejrup, H.P., Augedal, H., Jørstad, A., 2017. Late Pliocene-Pleistocene environments and glacial history of the northern North Sea. Quat. Sci. Rev. 158, 107–126. https://doi.org/10.1016/j.quascirev.2016.12.022.

Resnick, J.R., 1990. Stratigraphic filtering. Pure Appl. Geophys. 132 (1–2), 49–65. https://doi.org/10.1007/BF00874357.

Riboulot, V., Thomas, Y., Berné, S., Jouet, G., Cattaneo, A., 2014. Control of Quaternary sea-level changes on gas seeps. Geophys. Res. Lett. 41 (14), 4970–4977. https://doi.org/10.1002/2014GL060460.

Roberts, J.J., Wilkinson, M., Naylor, M., Shipton, Z.K., Wood, R.A., Haszeldine, R.S., 2017. Natural CO2 sites in Italy show the importance of overburden geopressure, fractures and faults for CO2 storage performance and risk management. Geol. Soc. London Spec. Publ. 458 (1), 181–211. https://doi.org/10.1144/sp458.14.

Roche, B., Bull, J.M., Marin-Moreno, H., Leighton, T., Falcon-Suarez, I.H., White, P.R., Provenzano, G., Tholen, M., Lichtschlag, A., Li, J., Faggetter, M., (in review, this volume). Time-lapse Imaging of CO_2 migration Within Near-surface Sediments during a Controlled Sub-seabed Release Experiment.

Ross, J.A., Peakall, J., Keevil, G.M., 2014. Facies and flow regimes of sandstone-hosted columnar intrusions: insights from the pipes of Kodachrome Basin State Park. Sedimentology 61 (6), 1764–1792. https://doi.org/10.1111/sed.12115.

Rost, S., Thomas, C., 2009. Improving seismic resolution through array processing techniques. Surv. Geophys. 30 (4–5), 271–299. https://doi.org/10.1007/s10712-009-9070-6.

Rutqvist, J., 2015. Fractured rock stress-permeability relationships from in situ data and effects of temperature and chemical-mechanical couplings. Geofluids 15 (1-2), 48–66. https://doi.org/10.1111/gfl.12089.

Saleem, U., 2020. Numerical Modeling of Two-phase Flow Through Porous Media Into Water Column. Chapter 6. PhD Thesis. Heriot-Watt University, Edinburgh, UK.

Schmidt, M., 2019. RV POSEIDON Cruise Report POS534 STEMM-CCS: Strategies for Environmental Monitoring of Marine Carbon Capture and Storage Leg 1: Kiel (Germany) – Aberdeen (United Kingdom) 01.05. – 22.05.2019 Leg 2: Aberdeen (United Kingdom) – Bremerhaven (Germany) 23.05. – 29.05.2019.

Schneider von Deimling, J.S., Greinert, J., Chapman, N.R., Rabbel, W., Linke, P., 2010. Acoustic imaging of natural gas seepage in the North Sea: sensing bubbles controlled by variable currents. Limnol. Oceanogr. Methods 8 (5), 155–171. https://doi.org/10.4319/lom.2010.8.155.

Seeberg-Elverfeldt, J., Schlueter, M., Feseker, T., Kolling, M., 2005. Rhizon sampling of porewaters near the sediment-water interface of aquatic systems. Limnol. Oceanogr. Methods 3, 361–371. https://doi.org/10.4319/lom.2005.3.361.

Shapiro, S.A., Hubral, P., 1995. Frequency-dependent shear-wave splitting and velocity anisotropy due to elastic multilayering. J. Seismic Explor. 4, 151–168. https://doi.org/10.1190/1.1444567.

Sinha, M.C., Patel, P.D., Unsworth, M.J., Owen, T.R.E., MacCormack, M.R.G., 1990. An active source electromagnetic sounding system for marine use. Mar. Geophys. Res. 12 (1–2), 59–68. https://doi.org/10.1007/BF00310563.

Sirgue, L., Barkved, O.I., Dellinger, J., Etgen, J., Albertin, U., Kommedal, J.H., 2010. Thematic set: full waveform inversion: the next leap forward in imaging at Valhall. First Break. 28 (4), 65–70. https://doi.org/10.3997/1365-2397.2010012.

Smith, A.J., Mienert, J., Bünz, S., Greinert, J., 2014. Thermogenic methane injection via bubble transport into the upper Arctic Ocean from the hydrate-charged Vestnesa Ridge, Svalbard. Geochem. Geophys. Geosyst. 15 (5), 1945–1959. https://doi.org/10.1002/2013GC005179.

Smithyman, B., Pratt, R.G., Hayles, J., Wittebolle, R., 2009. Detecting near-surface objects with seismic waveform tomography. Geophysics 74 (6), WCC119–WCC127. https://doi.org/10.1190/1.3223313.

Stewart, M.A., Lonergan, L., 2011. Seven glacial cycles in the middle-late Pleistocene of northwest Europe: geomorphic evidence from buried tunnel valleys. Geology 39 (3), 283–286. https://doi.org/10.1130/g31631.1.

Stoker, M.S., Balson, P.S., Long, D., Tappin, D.R., 2011. An overview of the lithostratigraphical framework for the Quaternary deposits on the United Kingdom continental shelf. Br. Geol. Surv. Res. Rep. 48. RR/11/03. http://nora.nerc.ac.uk/id/eprint/15939/1/RR11003.pdf.

Sun, Q.L., Cartwright, J., Wu, S.G., Chen, D.X., 2013. 3D seismic interpretation of dissolution pipes in the South China Sea: genesis by subsurface, fluid induced collapse. Mar. Geol. 337, 171–181. https://doi.org/10.1016/j.margeo.2013.03.002.

Tary, J.B., Géli, L., Guennou, C., Henry, P., Sultan, N., Çağatay, N., Vidal, V., 2012. Microevents produced by gas migration and expulsion at the seabed: a study based on sea bottom recordings from the Sea of Marmara. Geophys. J. Int. 190 (2), 993–1007. https://doi.org/10.1111/j.1365-246X.2012.05533.x.

Taylor, P., Stahl, H., Vardy, M.E., Bull, J.M., Akhurst, M., Hauton, C., James, R.H., Lichtschlag, A., Long, D., Aleynik, D., Toberman, M., 2015. A novel sub-seabed CO2 release experiment informing monitoring and impact assessment for geological carbon storage. Int. J. Greenh. Gas Control. 38, 3–17. https://doi.org/10.1016/j.ijggc.2014.09.007.

Thomsen, L., 1995. Elastic anisotropy due to aligned cracks in porous rock1. Geophys. Prospect. 43 (6), 805–829. https://doi.org/10.1111/j.1365-2478.1995.tb00282.x.

Tóth, J., 1980. Cross-formational gravity-flow of groundwater: a mechanism of the transport and accumulation of petroleum (the generalized hydraulic theory of petroleum migration). Probl. Pet. Migr. 121–167. https://doi.org/10.1306/St10411C8.

Tóth, Z., Spiess, V., Mogollón, J.M., Jensen, J.B., 2014. Estimating the free gas content in Baltic Sea sediments using compressional wave velocity from marine seismic data. J. Geophys. Res. Solid Earth 119 (12), 8577–8593. https://doi.org/10.1002/2014JB010989.

Tóth, Z., Spiess, V., Keil, H., 2015. Frequency dependence in seismoacoustic imaging of shallow free gas due to gas bubble resonance. J. Geophys. Res. Solid Earth 120, 8056–8072. https://doi.org/10.1002/2015JB012523.

Tucker, P.M., Yorston, H.J., 1973. Pitfalls in seismic interpretation. Geophys. Monogr. Ser. 57. https://doi.org/10.1190/1.9781560802365.

Vardy, M.E., 2015. Deriving shallow-water sediment properties using post-stack acoustic impedance inversion. Near Surf. Geophys. 13 (2), 143–154. https://doi.org/10.3997/1873-0604.2014045.

Vardy, M.E., Vanneste, M., Henstock, T.J., Clare, M.A., Forsberg, C.F., Provenzano, G., 2017. State-of-the-art remote characterization of shallow marine sediments: the road to a fully integrated solution. Near Surf. Geophys. 15 (4), 387–402. https://doi.org/10.3997/1873-0604.2017024.

Varela, I., Nasser, M., Chapman, M., Liu, E., 2006. Anisotropic azimuthal attenuation as an indicator of fracture properties, a case study on time-lapse walkaround VSP data. In: 68th EAGE Annual Conference and Technical Exhibition. European Association of Geoscientists & Engineers. https://doi.org/10.3997/2214-4609.201402333.

Virieux, J., Operto, S., 2009. An overview of full-waveform inversion in exploration geophysics. Geophysics 74 (6), WCC1–WCC26. https://doi.org/10.1190/1.3238367.

Waage, M., Bünz, S., Landrø, M., Plaza-Faverola, A., Waghorn, K.A., 2019. Repeatability of high-resolution 3D seismic data. Geophysics 84 (1), B75–B94. https://doi.org/10.1190/geo2018-0099.1.

Watson, T.L., Bachu, S., 2009. Evaluation of the potential for gas and CO2 leakage along wellbores. Society of Petroleum Engineers. https://doi.org/10.2118/106817-PA.

Watts, G.F.T., Jizba, D., Gawith, D.E., Gutteridge, P., 1996. Reservoir monitoring of the Magnus Field through 4D time-lapse seismic analysis. Pet. Geosci. 2 (4), 361–372. https://doi.org/10.1144/petgeo.2.4.361.

Weitemeyer, K.A., Constable, S., Tréhu, A.M., 2011. A marine electromagnetic survey to detect gas hydrate at Hydrate Ridge, Oregon. Geophys. J. Int 187 (1), 45–62. https://doi.org/10.1111/j.1365-246X.2011.05105.x.

Werner, U., Shapiro, S.A., 1999. Frequency-dependent shear-wave splitting in thinly layered media with intrinsic anisotropy. Geophysics 64 (2), 604–608. https://doi.org/10.1190/1.1444567.

White, J.E., 1975. Computed seismic speeds and attenuation in rocks with partial gas saturation. Geophysics 40 (2), 224–232. https://doi.org/10.1190/1.1440520.

White, R.S., 1977. Seismic bright spots in the Gulf of Oman. Earth Planet. Sci. Lett. 37 (1), 29–37. https://doi.org/10.1016/0012-821X(77)90143-1.

Whiteside, W., Wang, B., Bondeson, H., Li, Z., 2013. 3D imaging from 2D seismic data, an enhanced methodology. In SEG Technical Program Expanded Abstracts 2013. Soc. Explor. Geophys. 3618–3622. https://doi.org/10.1190/segam2013-1148.1.

Whitesides, G., 2006. The origins and the future of microfluidics. Nature 442, 368–373. https://doi.org/10.1038/nature05058.

Worthington, M.H., Hudson, J.A., 2000. Fault properties from seismic Q. Geophys. J. Int. 143, 937–944. https://doi.org/10.1046/j.1365-246X.2000.00315.x.

Yao, H., van Der Hilst, R.D., De Hoop, M.V., 2006. Surface-wave array tomography in SE Tibet from ambient seismic noise and two-station analysis—I. Phase velocity maps.

Geophys. J. Int. 166 (2), 732–744. https://doi.org/10.1111/j.1365-246X.2006.03028.x.

Zelt, C.A., Barton, P.J., 1998. Three-dimensional seismic refraction tomography: a comparison of two methods applied to data from the Faeroe Basin. J. Geophys. Res. Solid Earth 103 (B4), 7187–7210. https://doi.org/10.1029/97JB03536.

Zelt, C.A., Sain, K., Naumenko, J.V., Sawyer, D.S., 2003. Assessment of crustal velocity models using seismic refraction and reflection tomography. Geophys. J. Int. 153 (3), 609–626. https://doi.org/10.1046/j.1365-246X.2003.01919.x.